

# Mechanical Self-Assembly of a Strain-Engineered Flexible Layer: Wrinkling, Rolling, and Twisting

Zi Chen,<sup>1,\*</sup> Gaoshan Huang,<sup>2</sup> Ian Trase,<sup>1</sup> Xiaomin Han,<sup>1</sup> and Yongfeng Mei<sup>2,†</sup>

<sup>1</sup>*Thayer School of Engineering, Dartmouth College, Hanover, New Hampshire 03755, USA*

<sup>2</sup>*Department of Materials Science, Fudan University, Shanghai 200433, People's Republic of China*  
(Received 21 July 2015; revised manuscript received 5 November 2015; published 7 January 2016)

Self-shaping of curved structures, especially those involving flexible thin layers, is attracting increasing attention because of their broad potential applications in, e.g., nanoelectromechanical and microelectromechanical systems, sensors, artificial skins, stretchable electronics, robotics, and drug delivery. Here, we provide an overview of recent experimental, theoretical, and computational studies on the mechanical self-assembly of strain-engineered thin layers, with an emphasis on systems in which the competition between bending and stretching energy gives rise to a variety of deformations, such as wrinkling, rolling, and twisting. We address the principle of mechanical instabilities, which is often manifested in wrinkling or multistability of strain-engineered thin layers. The principles of shape selection and transition in helical ribbons are also systematically examined. We hope that a more comprehensive understanding of the mechanical principles underlying these rich phenomena can foster the development of techniques for manufacturing functional three-dimensional structures on demand for a broad spectrum of engineering applications.

DOI: 10.1103/PhysRevApplied.5.017001

## I. INTRODUCTION

The spontaneous bending, twisting, and wrinkling of thin layers are ubiquitous in both natural and synthetic systems. These phenomena have garnered significant interest from the scientific community because of their potential applications in sensors [1], actuators [2], microrobotics [3], nanoelectromechanical systems [4], active materials [5], optoelectronics [6], stretchable electronics [7], and drug-delivery systems [8]. These deformations often stem from a need to release potential energy in the presence of surface stresses [9], misfit strains [10], residual strains [11–13], thermal stresses [14], swelling and shrinkage [15,16], or differential growth [17,18]. As such, deformations are often triggered by environmental factors, such as humidity, temperature, and pressure. Significant research has been devoted to causing asymmetric deformation in thin layers under uniform environmental change, often by introducing some level of anisotropy into the system. This behavior allows the construction of systems that can have multiple complex responses to simple changes in scalar signals.

In synthetic thin structures, if a flexible layer is extended with a geometrically limited boundary, wrinkling or buckling in the perpendicular direction occurs. Strain engineering in a thin layer could produce a variety of three-dimensional (3D) structures besides wrinkles. For instance, self-rolling of a layer with a strain gradient can lead to the formation of tube or scroll-like structures [2]. Experimental and theoretical

investigations about formation mechanisms of these micro- and nanostructures have previously been carried out. With the rapid development of nanostructures and nanodevices, these structures are being pursued for many applications like flexible electronics, stretchable electronics, nanophotonics, robotics, and microfluidics.

Furthermore, helices can be considered as a special subclass of structures formed through rolling. They are chiral structures with broken left-right symmetry [19], which can be either left-handed or right-handed with a mirror image that has an opposite handedness or chirality. It is natural to think that such symmetry breaking comes from the chirality of the microscopic building units, but this is not always the case [12]. Spontaneous helical ribbons can form either under terminal loads (e.g., tensile forces or torques) [20] or in the absence of terminal loads [9,15,21–23]. Shape transitions between purely twisted ribbons (or helicoids), cylindrical helical ribbons, and tubules are frequently observed in twist-nematic elastomers [1,24], peptides [22,25], strained multi-layer composites [9,15,21–23], and nanoribbons [10,26]. These transitions are often driven by the complex interplay between molecular interactions, environmental stimuli, elastic properties, and nonlinear geometric effects.

Twisting can exist in thin layers outside of the uniform-helix-shape subclass and can occur even when the driving forces are not off axis with respect to the geometric axes of the material [12]. Twists in thin layers have an associated handedness and can even switch handedness [17]. Off-axis competition between the internal chirality of the building units of the thin layer and macroscopic forces acting on the layer can also form twists.

\*zi.chen@dartmouth.edu

†yfm@fudan.edu.cn

This article covers the analysis of these aforementioned deformation modes such as wrinkling, rolling, and twisting, along with examples and applications of each. This is followed by a synthesis of current promising research directions and future applications. Readers interested in the mechanics of thin-layer deformation are encouraged to refer to some excellent recent reviews for a more comprehensive understanding of recent developments [27–30].

Recently, wrinkling in nanoparticle films has received a great deal of attention. The most common films include graphene [31–33], nanocrystals [34–37], and nanotubes [38–40]. While the following discussion avoids focusing on nanoparticle films in depth, they are an important subset of wrinkling research, and the reader is encouraged to refer to those articles. It should also be noted that, while the discussion of wrinkling and rolling mechanics is primarily focused on inorganic materials, polymer sheets are becoming increasingly important in science and engineering. For a discussion of the specific mechanics of polymer surfaces, we point the reader to Rodríguez-Hernández's excellent review [41].

## II. SELF-ASSEMBLY AND STRAIN DISTRIBUTION IN WRINKLES

### A. Wrinkling versus rolling in a strain-engineered flexible layer

A flexible prestrained layer attached to a fixed boundary adopts a 3D structure in order to minimize strain energy [42–44]. Typical deformations reported in the literature include wrinkling [45,46], bending [43,44,47], folding [48–50], and ridging [51], depending on the strain gradient and magnitude. Normally, a small strain gradient produces wrinkles, while a large strain gradient makes the layer bend or roll into a curved structure [52]. Real materials are more complicated, as competition between bending and stretching energy can cause transitions between wrinkling and rolling states after the flexible layer is set free in one end and fixed in the other end.

Theoretical analyses have been carried out on both the wrinkling and rolling cases [29,42,52–60]. A simple analysis can be done by using an isotropically strained bilayer structure. Shown in Fig. 1 [52], the bilayer with thicknesses  $d_1$  and  $d_2$  is subjected to biaxial strain  $\varepsilon_1$  and  $\varepsilon_2$ , respectively. The bilayer is free hanging over a distance  $h$  and is initially in a strained state over the length  $L$ . The released portion is free to elastically relax, constrained only by the fixed boundary [see the dashed line in Fig. 1(a)] [52]. The average strain and strain gradient of the bilayer are defined as  $\bar{\varepsilon} = (\varepsilon_1 d_1 + \varepsilon_2 d_2)/(d_1 + d_2)$  and  $\Delta\varepsilon = \varepsilon_1 - \varepsilon_2$ , respectively, and  $\Delta\varepsilon > 0$ . The initial elastic energy (given per unit area) of the bilayer is  $E_0 = Y(d_1 \varepsilon_1^2 + d_2 \varepsilon_2^2)/(1 - \nu)$ , where  $Y$  and  $\nu$  are the Young's modulus and Poisson's ratio, respectively. In the bending case, the fixed boundary limits relaxation in the  $x$  direction, and the strain is relaxed via bending in the  $y$  direction to form a curved

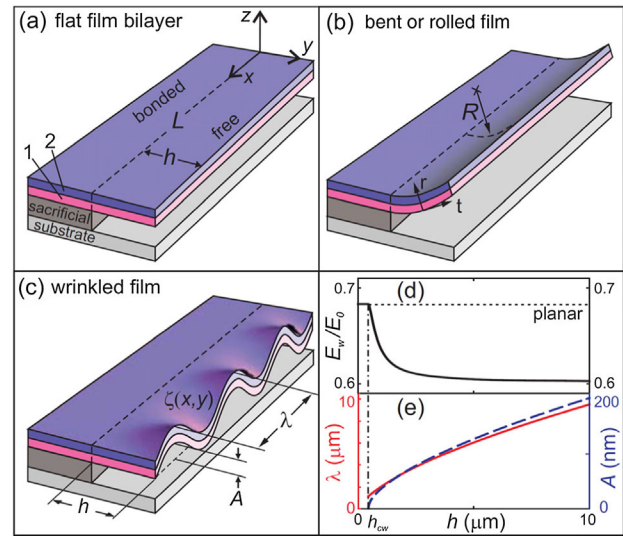


FIG. 1. Schematics of a (a) released bilayer, (b) bent bilayer with inner radius  $R$ , and (c) wrinkled structure with deflection profile  $\zeta(x, y)$ , amplitude  $A$ , and wavelength  $\lambda$ . (d)  $E_w$  (solid line) and energy of planar relaxation (dashed line) as a function of  $h$ . (e) Wavelength  $\lambda$  (solid line, left axis) and amplitude  $A$  (dashed line, right axis) as a function of length  $h$ , in the case of wrinkled structure. The vertical dotted-dashed line marks the  $h_{cw}$ . Reprinted with permission from Ref. [52] (© 2009 by the American Physical Society).

structure with inner radius  $R$  [Fig. 1(b)]. Since the layers are thin, the stress component in the radial direction (through the thickness direction) must be zero at equilibrium [61]. The total elastic energy of the bent film  $E_{\text{bent}}$  is calculated by integrating the elastic strain energy density from the outer to the inner film surface [52]. The equilibrium elastic energy of the rolled structure  $E_{\text{bent}}$  can be obtained by minimizing the energy and is normalized to  $E_0$  and then compared with the wrinkle energy  $E_w$  [52]. In the wrinkling case [Fig. 1(c)], the deflection of the bilayer can be written as a function  $\zeta = Af(y) \cos(kx)$ , where  $A$  is the maximum amplitude of the wrinkle at the free end,  $k$  is the wrinkle wave number in the  $x$  direction, and  $f(y) = [1 - \cos(\pi y/h)]/2$ . In the calculation of the wrinkle energy,  $E_w$  is averaged over one wavelength,  $L = \lambda$ , and  $L$  is numerically minimized with respect to  $A$ ,  $\lambda$ , and  $\gamma$  (where  $\lambda$  is the wavelength of the wrinkle and  $\gamma$  is the magnitude of relaxation in the  $y$  direction). The wrinkle energy as a function of the wrinkle length is given in Fig. 1(d), and it is found that there is a minimum critical wrinkle length  $h_{cw}$ , for wrinkle formation. The value of  $h_{cw}$  is  $h_{cw} \approx 2.57d_2\sqrt{-\bar{\varepsilon}}$  [52]. For  $h < h_{cw}$ , energy minimization provides only a trivial minimum of the wrinkle energy with  $A = 0$  and  $\lambda \rightarrow \infty$  [62], corresponding to a planar relaxation in the  $y$  direction [dashed line in Fig. 1(d)]. For  $h > h_{cw}$ , wrinkling can occur, and both  $\lambda$  and  $A$  increase with  $h$ , as demonstrated in Fig. 1(e). The preferred equilibrium shape of a free-hanging film could be found by comparing these two normalized energies,  $E_{\text{bent}}$

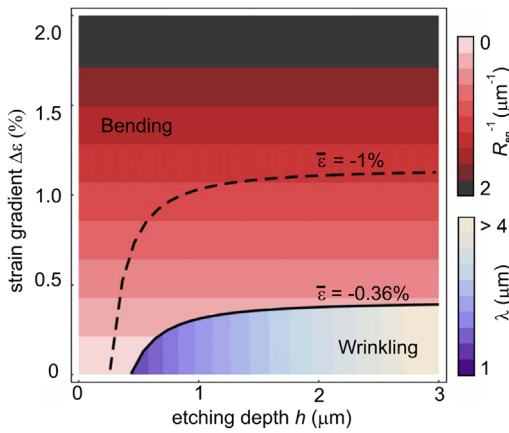


FIG. 2. Phase diagram of favorable shapes of a strained bilayer based on the energetic comparison between  $E_w$  and  $E_{bent}$ . The solid curve indicates the boundary separating the bent and wrinkled shapes.  $R_{eq}$  is shown for the bent structure and wavelength  $\lambda$  for the wrinkled structure. The dashed curve is the phase boundary curve for  $\bar{\epsilon} = -1.0\%$ . Reprinted with permission from Ref. [52] (© 2009 by the American Physical Society).

and  $E_w$ .  $h > h_{cw}$  does not guarantee wrinkle formation. Large  $h$  also allows the bilayer to roll if the strain gradient (or  $\Delta\epsilon$ ) is also large. A wrinkled structure is formed only when the strain gradient is small enough, even if  $h > h_{cw}$  [29,52]. For a typical bilayer consisting of 10 nm  $\text{In}_{0.1}\text{Ga}_{0.9}\text{As}$  and 10 nm GaAs, Young's modulus  $Y = 80$  GPa, and Poisson ratio  $\nu = 0.31$ , the  $\epsilon_1$  and  $\epsilon_2$  are systematically changed to calculate the favorable shape as a function of  $h$  and  $\Delta\epsilon$ , and the obtained phase diagram is shown in Fig. 2. When  $\Delta\epsilon = 0.20\%$  and  $\bar{\epsilon} = -0.36\%$ , bending is favored when  $h < 700$  nm. With larger  $h$ , the wrinkled structure has lower energy and is favorable [52]. The boundary between the two shapes is shown as a solid line in Fig. 2. For higher  $\bar{\epsilon}$  like  $-1.0\%$ , the phase-boundary curve moves upwards (see the dashed line in Fig. 2) and the wrinkling region is enlarged [52]. Figure 2 shows that for a wrinkled structure the wavelength  $\lambda$  increases with  $h$ , while for a bent structure the equilibrium radius  $R_{eq}$  decreases with increasing  $\Delta\epsilon$ . One should note that, at small length scales, the continuum theory may not always be accurate, as misfit dislocations in the boundary, surface properties, and size effects play an increasing large role.

For an anisotropically strained flexible layer, the situation is simpler. The coordinate system is the same as in Fig. 1(a). If the  $y$  direction is the most compliant direction, the layer bends or rolls in this direction [29]. If the  $x$  direction is the most compliant direction, deformation is dependent on  $h_{cw}$ . When  $h < h_{cw}$  the boundary [dashed line in Fig. 1(a)] does not allow the strain to relax along the  $x$  direction and the strain is retained, but when  $h > h_{cw}$  the released layer attempts to bend in the  $x$  direction and the constraint thus causes the wrinkles [29,42].

In the above investigation, only pure bending and pure wrinkling are considered, and the favorable shapes are

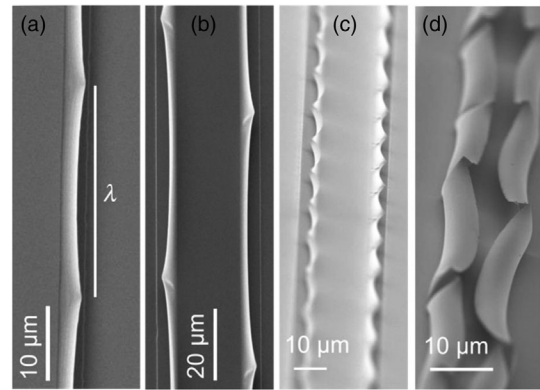


FIG. 3. Morphology evolution for increasing etching time. SEM images are shown for (a)  $h = 3.4 \mu\text{m}$  (top view); (b)  $h = 5.7 \mu\text{m}$  (top view); (c)  $h = 5.7 \mu\text{m}$  (side view) and (d)  $h = 10.3 \mu\text{m}$  (side view). Adapted from Ref. [64] with permission of The Royal Society of Chemistry.

decided by the energy minimization. However, experimental results sometimes show an obvious deviation from these theoretical predictions, and the parameters during release can considerably influence the final geometry [63]. For example, Figs. 3(a)–3(d) show the SEM images of the sample morphologies as a function of etching time, and the superposition of bending or rolling and wrinkling is obvious [64]. For an etching distance  $h = 3.4 \mu\text{m}$  [Fig. 3(a)], one can see a bent layer corresponding roughly to  $1/6$  of a tube circumference along with wrinkles of wavelength  $\lambda = 30 \pm 3 \mu\text{m}$  on its edge. For  $h = 5.7 \mu\text{m}$ , the released layer is rolled up to about  $1/3$  tube circumference, and the wrinkles have a wavelength of  $\lambda = 76 \pm 10 \mu\text{m}$  [Figs. 3(b) and 3(c)]. The layer with the etching distance of  $h = 10.3 \mu\text{m}$  is rolled up to about  $1/2$  tube circumference with large wrinkles of wavelength  $\lambda = 124 \pm 19 \mu\text{m}$ , as shown in Fig. 3(d). These results show the coexistence of rolling and wrinkling and demonstrate a large departure from previous analytical scaling predictions [64]. The strained bilayer is forced to accommodate both the rolled-up and the wrinkled morphology (due to the strain gradient and the average strain present in the bilayer) even though it is energetically the less favorable state. In such cases, a finite-element-method (FEM) simulation gives more accurate predictions. The anomalous results are believed to be the result of additional effects during the relaxation of a strained bilayer, such as stress focusing and capillary forces, which can have a significant effect but are not taken into account in the analytical calculations [64,65].

The relationship between bending and wrinkling can be more than just competition or coexistence. Researchers investigated the bending behavior after releasing an initially wrinkled layer and found that rolling parallel to wrinkle is more favorable due to the energy barrier existing in the calculation [65]. However, the external forces exerted during the fabrication process can strongly influence the final geometry [65]. While not discussed in this review, the

transition between wrinkling and crumpling is another important mechanism governed by primarily geometric constraints [66], especially in crystalline sheets [67].

### B. Internal and external control for a wrinkled layer

Practically, there are two methods frequently used to build and control wrinkling structures. The first approach, the internal control method, introduces internal strain into the active layer and is consistent with the aforementioned theoretical model. In 2007, Mei *et al.* [68] reported the formation of SiGe wrinkle arrays using this method. Briefly, a thin strained functional layer (e.g., SiGe layer) deposited onto a sacrificial buffer layer is partially released from the surface of the substrate by selectively etching off the sacrificial layer. Once the strained functional layer is freed from the substrate while one side is still fixed on the substrate, the strain elastically relaxes and causes wrinkles perpendicular to the etching front. The subsequent bond-back effect to the substrate leads to the formation of the ordered nanochannel network [Fig. 4(a)] [68]. Figure 4(b) shows the SiGe wrinkles formed with a straight etching front produced by photolithography or mechanical scratching. The network shown in the upper image in Fig. 4(b) consists of a single-sided branched channel network directly connected to the main channel. The middle image shows a double-sided branch nanochannel network, with the main channel running in between the wrinkled branch channels.

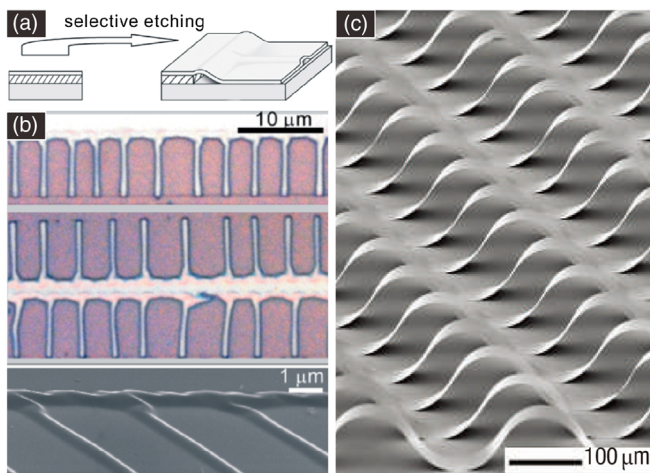


FIG. 4. (a) A schematic illustrating the formation of the wrinkles perpendicular to the etching front. The subsequent bond-back effect leads to the formation of a nanochannel network. Adapted with permission from Ref. [68] (© 2007). (b) Optical microscopy images showing a linear nanochannel network with single-sided (upper panel) and double-sided branch channels (middle panel). A corresponding SEM image (bird view) of a single-sided linear nanochannel network is given in the lower panel. Adapted with permission from Ref. [68]. (c) Si ribbon structures formed on a PDMS substrate prestrained to 50%. Reprinted with permission from Macmillan Publishers Ltd: Nature Nanotechnology, Ref. [69] (© 2006).

Figure 4(b) is a top-down SEM and shows that the open branch channel ends are arcs 300–500 nm wide and 120 nm high. The geometry of the wrinkle (channels with an arc-shaped cross section) deviates from the ideal case used in the theoretical calculation, and the measured periodicity is smaller than the value predicted by the calculation [68]. This discrepancy is due to the interaction between the free-hanging film and the substrate once the wrinkling amplitude becomes larger than the thickness of the sacrificial layer (which was not considered in the previous model). If the wrinkled film partially bonds back to the surface of the substrate, the layer cannot adapt its equilibrium periodicity, resulting in a decrease of practical periodicity. However, the film is not expected to tightly bond back to the surface during underetching, making the periodicity increase with a longer etching length. Although the wrinkles in the present case are not ideally sinusoidal due to the bond-back effect, the channels formed may have important applications in micro- and nanofluidics and biology [68]. Since the wrinkles are perpendicular to the etching front and the etching front can be well defined by conventional photolithography, complex channel arrays can be produced [69]. Malachias *et al.* [69] find that, in the two-dimensional (2D) case, the self-assembly of the channels is influenced by the shape, size, spacing of the etching start windows, and layer thickness. Under optimal conditions, ordered micro- or nanochannel arrays could be formed.

By contrast, the second approach, the external control method, does not require the release of the functional layer from the substrate. In this approach, the substrate is compressed or shrunk, and the surface functional layer is “expanded” related to the substrate, causing wrinkles [70,71]. A typical wrinkle structure produced by using this approach is shown in Fig. 4(c). To produce ordered wrinkle arrays, Sun *et al.* [70] patterned surface chemical adhesion sites on prestrained polydimethylsiloxane (PDMS) substrate by UV-light illumination through a photomask. Exposure to UV light creates patterned areas of ozone proximal to the surface of the PDMS [72]. The ozone converts the unmodified hydrophobic surface to a highly polar and reactive surface (activated surface), which allow various inorganic surfaces to form strong chemical bonds [73]. The unexposed sections therefore interact only weakly with other surfaces [74]. The inorganic ribbons (here, Si) are transferred to the treated PDMS substrate after baking in an oven at 90 °C for 5 min. Heating facilitates conformal contact and the formation of strong siloxane linkages between the activated areas of the PDMS and the native SiO<sub>2</sub> layer on the Si ribbons. Relaxing the strain in the PDMS leads to the formation of Si wrinkles through the physical separation of the ribbons from the inactivated regions of the PDMS [70]. The geometry of the wrinkles produced is tunable by changing the size and distribution of the activated regions. Inorganic semiconductor wrinkles have important applications in flexible electronics and

stretchable electronics shown by the works from the Rogers group at the University of Illinois at Urbana-Champaign [75–77].

It is worth pointing out that the external control method is not limited to relaxing prestrained substrates [78,79]. Processes which produce substrate deformation may also be used. Bowden *et al.* [80] find that wrinkles in thin metal films form due to thermal contraction of an underlying substrate. In fact, wrinkles can be easily produced on a treated PDMS substrate. Chung *et al.* [81] report plasma-assisted wrinkle formation. The process includes (i) heating the PDMS; (ii) exposing the PDMS to oxygen plasma to obtain a thin film of silicalike materials; and (iii) cooling down to generate the wrinkles. The wavelength and amplitude of wrinkles can be controlled by the heating temperature and time of plasma treatment. Generally, a higher temperature induces larger strain, leading to larger wrinkle amplitude. Increased exposure time thickens the silicalike layers and affects both the wavelength and the amplitude [81].

### C. Strain distribution of wrinkled layers: Neutral plane

A prestrained flexible layer can form wrinkled structures when minimizing its elastic energy [52,54,59,64,68]. But it is worth noting that the final wrinkled structure is not strain-free. Because of the curved flexible layer, the strain has a distribution profile along the depth. This distribution can be simulated by FEM or analytically modeled by considering the geometry before and after wrinkling [82,83]. In this section, we specifically discuss experimental results about strain distribution in wrinkles. The position of the neutral plane (where strain is zero) is a key point in this part.

In a simplified model [84,85] with a curved layer of thickness  $t$  and curvature  $r$ , the peak strain is given by

$$\varepsilon = \frac{t}{2r} \times 100\%. \quad (1)$$

The strain is compressive on one surface and tensile on the other, with an approximately linear variation between the two extremes and the neutral plane in the middle [85]. The location of the neutral plane is crucial for designing flexible electronics, since the device layer should be there to avoid destructive bending [86]. For a device fabricated on the surface of a substrate (e.g., PDMS), the addition of a compensating layer on top is necessary to adjust the location of the neutral plane. Kim *et al.* [86] use the method to calculate the location of the neutral plane in a multilayer system. For layers from 1 to  $n$  with a strain moduli of  $E_1, \dots, E_n$  and thicknesses of  $t_1, \dots, t_n$ , the neutral plane can be characterized by a distance  $d$  from the top surface and  $d$  is given by

$$d = \frac{\sum_{i=1}^n E_i t_i [(\sum_{j=1}^i t_j) - \frac{t_i}{2}]}{\sum_{i=1}^n E_i t_i}. \quad (2)$$

However, the real geometry of the 3D structure may deviate from the theoretical simulation (e.g., the bond-back

effect [68]), making calculations not always accurate. In addition, the experimental evidence of the strain distribution can rarely be directly obtained, especially in a very thin flexible layer. Optical methods are an effective way to probe the strain status in materials, although they are indirect methods that then need further fitting. Since the strain modifies the band structure of materials, the light emission from a wrinkled light-emitting layer can change. Luminescent  $\text{In}_{0.1}\text{Ga}_{0.9}\text{As}$  quantum wells (QWs) are embedded into a GaAs nanomembrane and act as both a local strain sensor and a strain source, and therefore the shift of QW emission indicates the strain state in the layer after the formation of a wrinkle [87]. After the mechanical relaxation, different emission wavelengths from different regions can be detected: The emission from the under-etched region is strongly redshifted with respect to the unetched region, and the bonded-back region exhibits the longest wavelength [87]. The lattice deformations and strain states in an unetched layer and in a wrinkled layer, including the bonded-back and the wrinkled regions, are schematically displayed in Fig. 5(a). The as-grown  $\text{In}_{0.1}\text{Ga}_{0.9}\text{As}$  QW has a thickness below the critical value for a dislocation introduction, and therefore the compressive strain is fully confined in the QW layer before etching [left panel in Fig. 5(a)]. After etching the layer, the bonded-back region is released from the substrate and partially relaxes its internal strain. The equilibrium configuration is between the fully strained QW (without tensile strain in the barrier layers) and the fully relaxed QW (with high tensile strain in the barrier layers), and tensile strain 0.237% exists in the barrier layers (above and below the QW layer) due to strain energy minimization [see the middle panel in Fig. 5(a)] [47,87]. For the wrinkled case in the right panel in Fig. 5(a), the bending of the nanomembrane generates an inhomogeneous strain distribution where the lattice constant in the growth direction depends on the inner lattice constant and the curvature, and the strain distribution varies linearly with the distance from the inner wrinkle surface to the outer surface [87]. By assuming a position for the neutral plane (dotted line, indicating no change of the strain state before and after bending) [61], the residual forces can be obtained, which can be tensile or compressive as shown in the right panel in Fig. 5(a). Based on the strain status and linear deformation potential theory [88], the band diagram and the energy levels of the QW can be obtained, as shown in Fig. 5(b). The transition energies are 1.3762, 1.3638, and 1.3683 eV for strained, partially relaxed, and wrinkled regions, respectively [87]. In order to gain more insight into the strain status of the wrinkle layer, the dependence of the calculated transition energies on the curvature is shown in Fig. 5(c) for three different models. The first model assumes strain energy minimization at a fixed curvature (bent QW I). The second model assumes that the neutral plane is sitting at the center of the QW (bent QW II). In contrast, a variable position of the neutral plane is

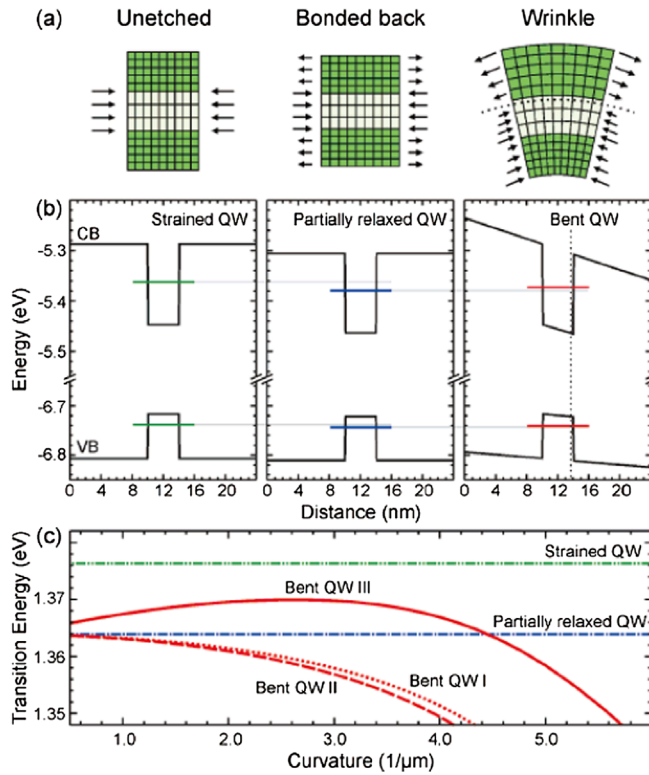


FIG. 5. (a) Schematic of the unetched (strained QW), bonded-back (partially relaxed QW), and wrinkled (bent QW) structures. (b) Band diagram and quantized energy levels corresponding to the structure shown in (a). Light gray lines are guides to the eye. (c) Transition energy of the bent QW as a function of the bending curvature. Three bent QW models are presented. Reprinted with permission from Ref. [87] (© 2007 American Chemical Society).

considered as a fitting parameter in the third model (bent QW III). Figure 5(c) shows transition energies for strained and partially relaxed QWs. The first two models indicate only a redshift of transition energy compared to that of the partially relaxed region and, therefore, are inconsistent with the experimental results. Only the third model where the position of the neutral plane is varied gives consistent results in the curvature range of  $1\text{--}2\ \mu\text{m}^{-1}$ . Figure 5(c) indicates that the wrinkles result in a complicated strain state, which is possibly due to the external forces originating from the bond-back effect during the drying process [47,87].

Since Raman scattering is very sensitive to the internal strain of the flexible layer, Guo *et al.* [71] also carry out Raman mapping experiments on a wrinkled Si layer (on a PDMS substrate) to investigate this complex strain distribution. To probe the strain distribution along the depth, two lasers (514 and 325 nm) are used as Raman excitation sources. Typical color-coded Raman peak (Si-Si TO phonon) positions extracted from mappings using the two excitation sources are shown in Figs. 6(a) and 6(b), respectively. The peak position, i.e., the strain status at the point probed, shows periodic alternation along the  $x$  direction while keeping constant along the  $y$  direction. After the two images are aligned, it is striking to observe that the locations of the crest lines (i.e., the maximum wave number) of Raman mapping measured by the 514-nm laser correspond exactly to the valley lines (i.e., the minimum wave number) of the counterpart obtained by the 325-nm laser [71]. In order to simplify further investigation, a line cut along the  $x$  direction is performed, as shown in Figs. 6(c) and 6(d). The experimental results present the

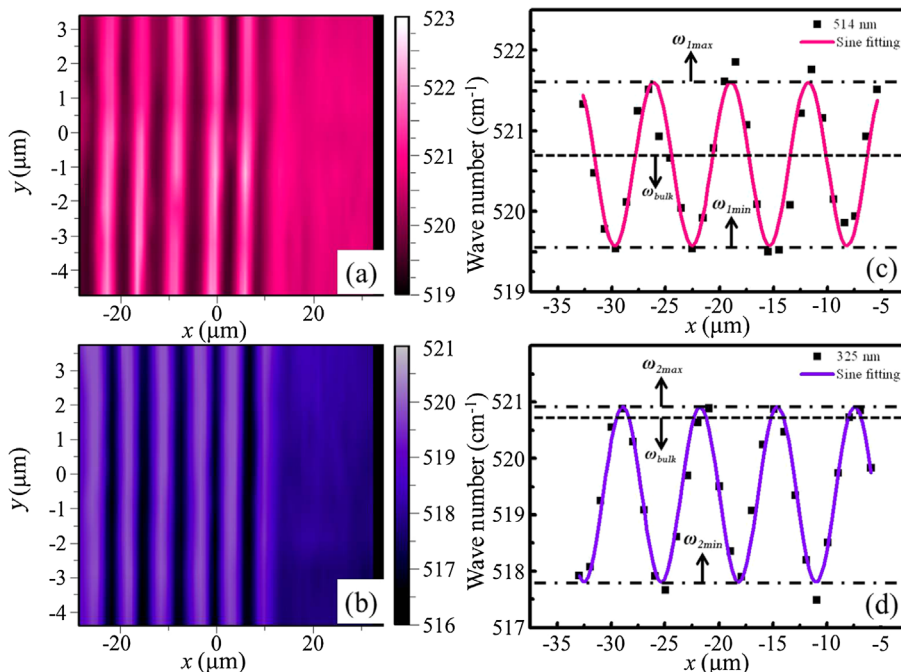


FIG. 6. Micro-Raman mapping measurements of the wrinkled Si layer, and the corresponding section analysis: (a),(c) 514-nm laser; (b),(d) 325-nm laser. Reprinted with permission from Ref. [71] (© 2013, AIP Publishing LLC).

typical sinusoidal shape, consistent with a computed fit to a sine function, shown by the solid line. The periodicity of the peak positions along the  $x$  direction is similar to that obtained from morphological characterization [71]. For the results obtained with the 514-nm laser, the Raman peak of unstrained bulk Si  $\omega_{\text{bulk}} = 520.7 \text{ cm}^{-1}$  is found in the middle of the sine curve [dotted line in Fig. 6(c)]. In the 325-nm laser case [Fig. 6(d)], the maximum wave number ( $\omega_{2\text{max}}$ ) decreases significantly and approaches  $\omega_{\text{bulk}}$ , and the minimum wave number ( $\omega_{2\text{min}}$ ) becomes much smaller than  $\omega_{\text{bulk}}$ . Since the detection depth of a Raman signal correlates with the wavelength of the excitation laser, it is believed that the above phenomenon results from the inhomogeneous strain distribution along the depth of the Si layer [71].

To simplify the theoretical analysis of the strain distribution, the Si layer and PDMS substrate system is separated into two basic elements: the suspended Si wrinkle and the unattached elastomeric PDMS substrate in a wrinkled shape. For the suspended Si wrinkle, the von Kármán elastic nonlinear plate theory [61,84,89] is used, so the dominant strain distribution in the deformed wrinkles is

$$\varepsilon_{xx}(x, y, z) = \varepsilon_{xx}^0 + \frac{\partial u_x}{\partial x} + \frac{1}{2} \left( \frac{\partial w_x}{\partial x} \right)^2 - \frac{1}{2} \frac{\partial^2 w_x}{\partial x^2} z, \quad (3)$$

where  $\varepsilon_{xx}^0$  is the initial strain (the compressive strain due to the relaxation of prestrain in PDMS, approximately 4.87% for the present case),  $u_x$  denotes the in-plane displacements in the  $x$  direction,  $w_x$  is the deflection of the Si layer which can be written as  $w_x = A \cos(kx)$ ,  $k = (2\pi)/\lambda$ , where  $A$  and  $\lambda$  are the amplitude and the wavelength of the wrinkle, respectively, and  $z$  is the distance to the center of the wrinkles. The uniform nature of strains suggests that the in-plane displacement should be written as [90]

$$u_x = \frac{1}{8} k A^2 \sin(2kx). \quad (4)$$

Then the strain field can be written as

$$\varepsilon_{xx}(x, y, z) = \varepsilon_{xx}^0 + \frac{1}{4} k^2 A^2 + \frac{1}{2} A k^2 \cos(kx) z. \quad (5)$$

The strain distribution is tuned by  $\cos(kx)$  and  $z$ . At the crest or the valley of the wrinkle,  $\cos(kx)$  is equal to  $+1$  or  $-1$ , and the depth distribution of the strain varies as  $z$  changes. The PDMS substrate also plays a significant role in the deformation. Shearing forces at the Si layer and PDMS interface cause tension at the valley and compression at the crest, resulting in a displacement of the neutral plane. Figure 7 shows the forces in the crest and valley of the sheet, with tensile strain on the top and compressive strain on the bottom. The neutral plane, where  $\varepsilon_{xx}(x, y, z) = 0$ , is negative at the crest and positive at the valley [71].

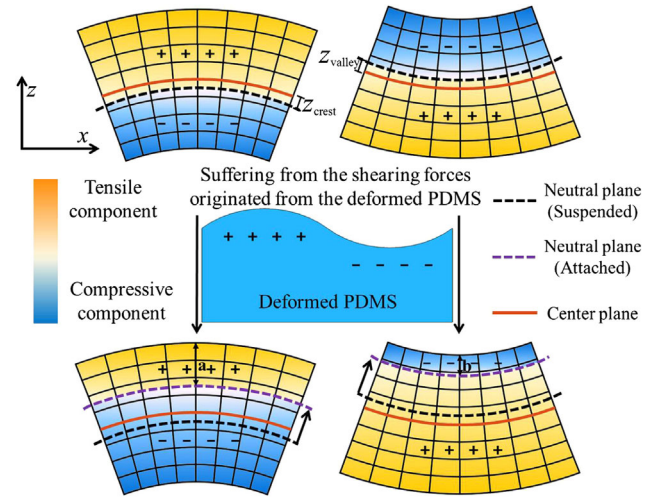


FIG. 7. Theoretical model for the strain distribution in the wrinkled silicon layer. Reprinted with permission from Ref. [71] (© 2013, AIP Publishing LLC).

The detection depth of the Raman system is determined by the wavelength of the excitation source [91]. A 325-nm laser can penetrate only 8 nm (1/3 of the total thickness) in Si, but a 512-nm laser can fully penetrate the sample. Crests generate a high-wave-number TO mode, while valleys generate a low one. The strain is also asymmetric, with the magnitude of compression at the crest higher than the tension in the valley [Fig. 6(c)]. This phenomenon is exacerbated when using a 325-nm laser, as the neutral plane of the crest is similar to the maximum penetration depth. The wave number at the crest ( $\omega_{2\text{min}}$ ) becomes much lower than it should be, while the valley wave number ( $\omega_{2\text{max}}$ ) stays close to  $\omega_{\text{bulk}}$  [Fig. 6(d)] [71].

### III. FABRICATION AND MODELING OF SELF-ROLLED-UP TUBES

#### A. Mechanical self-assembly of rolled-up tubes: Materials and fabrication

Strain gradients in a flexible layer can cause bending along the direction with the smallest Young's modulus, through energy minimization [92,93]. Specifically, as shown in Fig. 8, a strained bilayer is produced with its top layer in-plane compressed and its bottom layer tensilely stressed. When the sacrificial layer is selectively etched away, the strained bilayer becomes detached from the substrate. Its top layer contracts, while its bottom layer expands, which results in rolling [94]. If the shape of the layer is adapted to this rolling direction, micro- or nanotubes can be formed as shown in Fig. 8 [44,94,95]. In previous literature, several approaches have been proposed to introduce the necessary strain gradient or strain difference into flexible layers with a bi- or multilayered structure, which will be discussed in the following.

The first method utilizes lattice mismatch in an epitaxial bi- or multilayer structure. The advantage of this method is

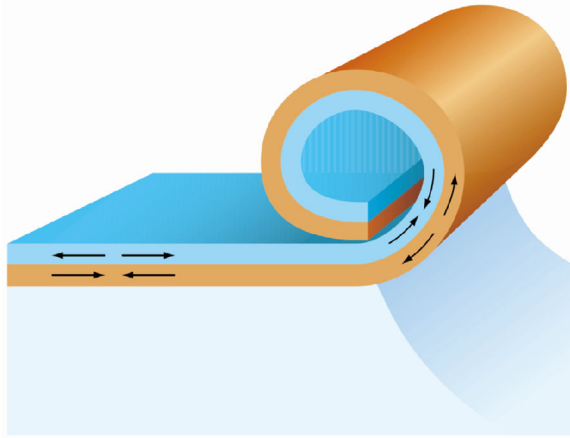


FIG. 8. When a bilayer is freed, its top layer contracts, and its bottom layer expands, causing the bilayer to roll up. From Ref. [96], reprinted with permission from AAAS.

that the strain gradient can be well controlled and thus the tube diameter is tunable (see the discussion later). If the thickness of the layer is smaller than the critical value, the layer is coherent, and one can easily calculate the strain gradient based on the well-known values of the lattice constants [97,98]. For instance, a Ge layer epitaxially grown onto a Si(001) substrate creates a 4% misfit strain at the interface if the Ge is fully strained [29]. In compound semiconductor materials, the lattice constant varies with the material composition and thus allows strain tuning. Not only group IV [44,95,99,100], but also group III-V [101–103], and even II-VI [104] semiconductor materials have been strain-engineered and rolled into a tubular geometry. However, in thick layers, this method is inaccurate, because the layer can be plastically relaxed via dislocations and the strain gradient cannot be well calculated by considering only lattice mismatch.

Other methods may also be used to introduce a strain gradient, but quantitative determination of the strain is difficult. The strain normally depends on experimental parameters during layer growth or deposition which can be manipulated to generate the required gradient [105]. For instance, the nonepitaxial vapor deposition of thin layers may also be inherently strained [29]. In addition, it was found that the heating or cooling of materials with different thermal expansion coefficients can introduce strain into the layers [29]. By changing the experimental conditions, Mei *et al.* [94] prepare microtubes from flexible layers. As shown in Fig. 9, prestressed inorganic layers deposited onto polymer sacrificial layers (here, photoresist) are released by removing the sacrificial layer with acetone or other organic solvents and roll up into microtubes. Since the sacrificial layer is organic and can be easily removed by organic solvents, flexible layers of almost any inorganic material can be rolled. Figures 9(a)–9(h) show examples of rolled-up microtubes: (a) Pt, (b) Pd/Fe/Pd, (c) TiO<sub>2</sub>, (d) ZnO, (e) Al<sub>2</sub>O<sub>3</sub>, (f) Si<sub>x</sub>N<sub>y</sub>, (g) Si<sub>x</sub>N<sub>y</sub>/Ag, and (h) diamondlike

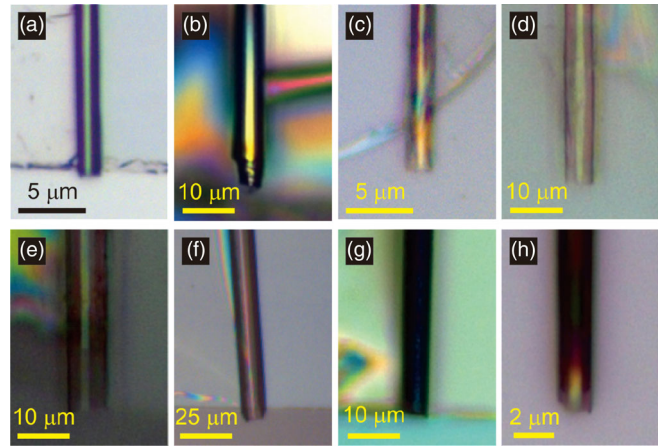


FIG. 9. Optical images of rolled-up microtubes made out of (a) Pt, (b) Pd/Fe/Pd, (c) TiO<sub>2</sub>, (d) ZnO, (e) Al<sub>2</sub>O<sub>3</sub>, (f) Si<sub>x</sub>N<sub>y</sub>, (g) Si<sub>x</sub>N<sub>y</sub>/Ag, and (h) diamondlike carbon. Adapted with permission from Ref. [94] (© 2008).

carbon [94]. Moreover, the photoresist sacrificial layer can be easily patterned by using conventional photolithography, and the flexible layer is replicated from the pattern during deposition, which is convenient for future device fabrication. Here, the layers are deposited by nonepitaxial methods, and it is believed that the strain gradient is introduced by a combination of substrate temperature evolution, deposition rate, and base pressure during deposition [94]. In multicrystal layers, different grain sizes in the flexible layer exert different strain levels [106].

It is worth noting that, although they are not commonly used, there are other approaches reported to introduce a strain gradient into a flexible layer. Theoretical investigation proves that surface reconstruction can create a strain gradient: A (2 × 1)-type reconstruction of a Si(001) surface can create a self-driving force that bends the Si layer [107]. In polymers, distinct swelling properties of chemically dissimilar polymers in solvents can provide the strain gradient needed for bending [108]. For instance, polystyrene (PS) and poly(4-vinylpyridine) (P4VP) can be dip-coated on a Si substrate to form a bilayer structure. Upon exposure to water, PS demonstrates minimal water uptake, forming a stiff hydrophobic layer. P4VP is relatively less hydrophobic and swells in acidic aqueous solutions because of the protonation of polymer chains [108,109]. This mechanical effect is successfully employed for rolling microtubes [110].

## B. Mechanical self-assembly of rolled-up tubes: Modeling

The rolling of a flexible layer is a mechanical self-assembly process. To construct a complex 3D structure, the rolling direction and its misalignment with the crystal orientation of the flexible layer should be carefully considered. If the strain gradient is fixed, the mechanical properties

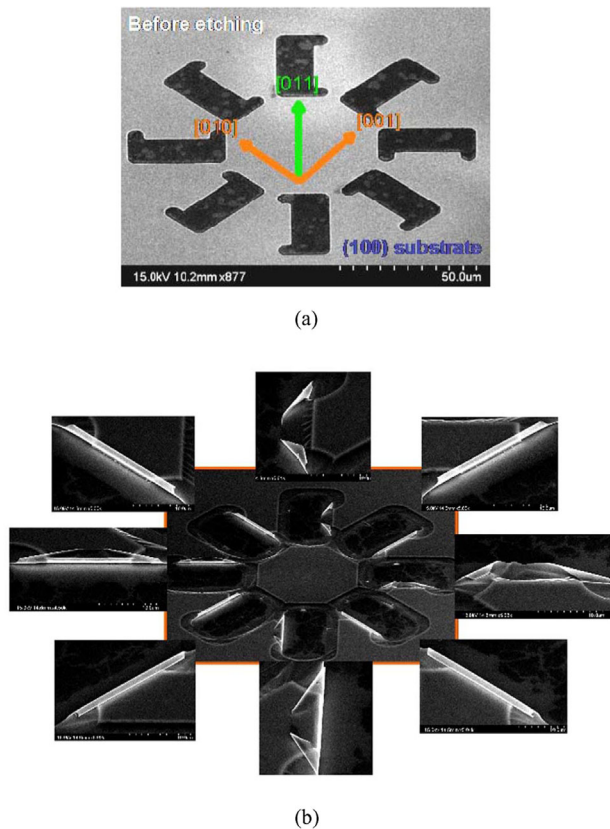


FIG. 10. A patterned wheel of anchored rectangular pads (a) before and (b) after lithography in SEM, with magnified pads displayed in (b).  $\text{In}_{0.3}\text{Ga}_{0.7}\text{As}/\text{GaAs}$  film is grown on (100) GaAs. Reprinted with permission from Ref. [114] (© 2008 IEEE).

of the layer influence the rolling direction significantly. In a single-crystal epitaxial layer, anisotropy in the crystal structure leads to anisotropic mechanical properties [58]. For instance, the Young's moduli in the GaAs  $\langle 100 \rangle$  and  $\langle 111, 112 \rangle$ . The Young's moduli in Si along the  $\langle 100 \rangle$  and  $\langle 110 \rangle$  directions are 130.2 and 168.9 GPa, respectively [113]. A calculation by energy minimization shows that rolling along the direction with the smallest Young's modulus (the softest direction) is preferred [58]. To

demonstrate this phenomenon experimentally, Chun and Li [114] design a wheel pattern with eight anchored stripe pads oriented symmetrically in the  $\langle 100 \rangle$  and  $\langle 110 \rangle$  directions [Fig. 10(a)]. The results of the  $\text{In}_{0.3}\text{Ga}_{0.7}\text{As}/\text{GaAs}$  bilayers released from the (001) GaAs substrate are shown in Fig. 10(b). The center image shows all pads around the wheel, and the enlarged image for each pad is laid out in the outer periphery. The four pads with longer edges oriented along the  $\langle 100 \rangle$  directions (diagonal lines of the wheel) form tubes, with rolling taking place in the  $\langle 100 \rangle$  direction and stopping at the foot anchors. For those four oriented along the  $\langle 110 \rangle$  directions, the rolling still occurs in the  $\langle 100 \rangle$  directions and thus forms "turnover" triangular patterns. The persistent rolling along the  $\langle 100 \rangle$  direction, regardless of how the rectangle stripe patterns are oriented, proves the anisotropy of stiffness in cubic GaAs crystals [114]. On the other hand, if the layer is fabricated by a nonepitaxial method, there is no anisotropy from the crystal structure, but it is found that the softest direction is that perpendicular to the deposition direction [115].

Chun *et al.* [63] specifically investigate the rolling behavior of the rectangular layer, where both sides are the softest directions, and the results are summarized in Fig. 11. The rolling direction is plotted as a function of three parameters:  $b/a$ ,  $c/a$ , and  $a$ , where  $a$  is the length of the rectangular membrane,  $b$  is the width, and  $c$  is the circumference of the tube. There are three types of rolling behavior observed in the experiment. The blue and red dots represent long-side rolling and short-side rolling, respectively, and the green dots are mixed cases with some tubes rolled up from the long side and some from the short side. Figure 11 shows that the rolling direction depends on not only the dimension of the starting layer ( $a$  and  $b$ ) but also the tube circumference ( $c$ ). Rolling occurs exclusively on the long side when ( $c/a > 2$ ) or ( $b/a > 9$ ) but is mixed when ( $c/a \ll 1$ ) and ( $b/a$ ) is low. Mixed and short rolling are also more likely to occur in sheets of a larger size [63].

In an experimental study, researchers notice that chemical etching anisotropy may also impact the rolling behavior [58]. Time evolution of rolling shows a complicated process [63]. The final rolling direction depends on the

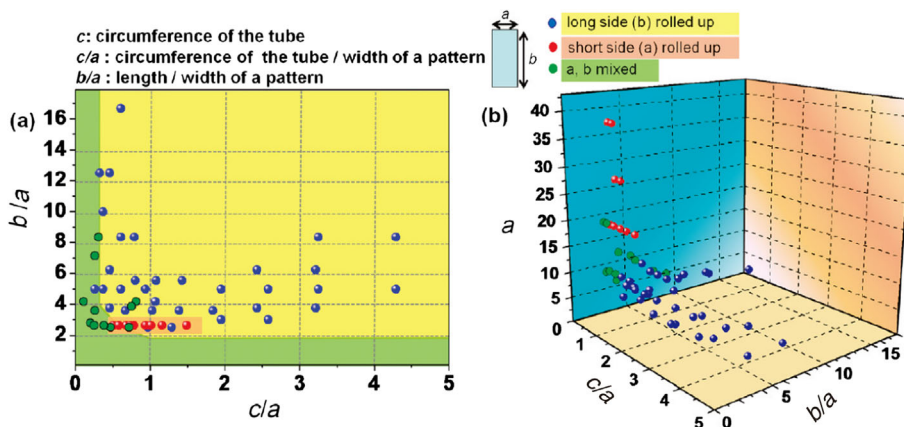


FIG. 11. Two- and three-dimensional plots of the rolling direction as a function of the tube circumference ( $c$ ), width ( $a$ ), and rectangular layer length ( $b$ ). Blue indicates long side rolling, red short side, and green for a combination. Adapted with permission from Ref. [63] (© 2010 American Chemical Society).

length and width of the layer, the energy of the final state, the history of the rolling process, the kinetic control of the etching isotropy, and the diameter of the tube [63].

The modeling of the tube geometry is another important concern. Considering the spiral cross section of rolled-up tube, one can calculate the number of rotations  $N$  as [116]

$$N = -(r/d - 1/2) + \sqrt{(r/d - 1/2)^2 + L/(\pi d)}, \quad (6)$$

where  $L = \sum_{n=1}^N 2\pi[r + (n-1)d]$  is the rolling distance,  $d$  is the layer thickness, and  $r$  is the tube radius of the initial turn [116]. The initial diameter and radius, on the other hand, should be determined by the strain gradient, the hardness, and the thickness of the layer. A few models have been proposed in previous literature. For a bilayer structure, the diameter  $D$  can be calculated based on a macroscopic continuous mechanical model [103,117] using the equation

$$D = \frac{d\{3(1+m)^2 + (1+m \cdot n) \cdot [m^2 + (m \cdot n)^{-1}]\}}{3\varepsilon(1+m)^2}, \quad (7)$$

where  $d = d_1 + d_2$  is the total thickness of the bilayer,  $\varepsilon$  is the in-plane biaxial strain between the two layers,  $n = Y_1/Y_2$  is the ratio of Young's modules, and  $m = d_1/d_2$  is the ratio of the thicknesses of the two layers. In 2006, Songmuang, Deneke, and Schmidt [118] proposed a slightly modified model based on their tube which rolled from a partially strain-relaxed single-material layer. In such a case, the layer is divided into two regions: The lower region close to the sacrificial layer experiences either a tensile or a compressive strain, and the upper layer is relaxed. The diameter of the tube can be described by [55,118]

$$D = \frac{1}{3\varepsilon} \frac{1}{d_1 d_2} (d_1 + d_2)^3. \quad (8)$$

It should be mentioned that the Poisson's ratio may also be considered if the material has anisotropic mechanical properties [118]. Investigations show that calculated diameters from these models agree well with the experimental results [103,119,120], although FEM may give even more accurate predictions. The imperfections of the above models are possibly due to a thickness deviation or additional strain [58]. The strain relaxation along the tube axis, as probed by x-ray diffraction [121] and optical characterization [122], may also influence the rolling process and tube geometry.

#### IV. MECHANICS AND GEOMETRY IN SELF-ASSEMBLED HELICAL STRUCTURES

##### A. Self-assembly of amphiphilic aggregation

Chirality, or handedness, is of key importance in many physical and chemical systems. Molecular interactions, for example, are often strongly dependent on the chirality of

the constituent molecules [123]. Helices are typical examples of chiral structures [19]. The self-assembly of helical structures, such as amphiphilic aggregates, is ubiquitous in natural and engineering systems and has since served as an efficient, "bottom-up" way of manufacturing nanostructures. For example, lipid bilayers can self-assemble into helices driven by  $\text{Ca}^{2+}$ -mediated intermembrane binding [124]. Helical ribbons that arise through the packing of amphiphilic molecules have since been investigated through both experiments and theoretical modeling [123,125–130].

Many molecules self-assemble in aqueous environments into larger aggregates, which can exhibit a variety of geometric shapes, from vesicles to twisted ribbons. Based on the continuum theory, Helfrich and Prost develop a theoretical model for the bending of anisotropic membranes to interpret the formation of tubes and helical ribbons from different amphiphiles [131]. By assuming that the chiral molecules are packed with some twist with respect to the nearest neighbors, the theory shows that this molecular twist can be propagated throughout the membrane, thus creating a bending force that results in the formation of helical ribbons or tubules. Later, Ouyang and Liu [132] follow this membrane elasticity approach but introduce a linear term by viewing chiral lipid bilayers as cholesteric liquid crystals to study the helical structures. The analysis shows that a twisted-ribbon shape and a helix with a  $45^\circ$  angle form as intermediate states before transitioning into tubes, consistent with previous experimental observations [132]. However, more recent experiments demonstrate that helical ribbons can be stable states and that the helix angle is not necessarily  $45^\circ$  [133].

Chung *et al.* [126] make perhaps the first attempt to interpret the appearance of different helix angles through a theoretical approach. Subsequently, Selinger and Schnur further develop a theoretical model, based on Helfrich and Prost's continuum theory, to find that the molecular chirality or tilt can result in the helical winding of a membrane and the radius can be predicted in terms of the continuum parameters [134] (Fig. 12). Soon afterwards, Selinger and co-workers extended this theory and considered membrane anisotropy to interpret the possibility of modulated state of tubules [Fig. 12(c)]. Yet another contribution from Selinger *et al.* [129] is to show that helical ribbons can actually be equilibrium configurations instead of being just intermediate states.

##### B. Mechanical self-assembly of helical ribbons: Microfabrication

Helical ribbons are an important set of geometric shapes among chiral structures. Such shapes often arise as a result of the competition between bending and in-plane stretching energy driven by certain internal or external forces. The sources of driving forces include, but are not limited to, surface stresses [9,135,136], residual stresses [137], misfit strains [10,138–140], molecular tilt [123,129,141],

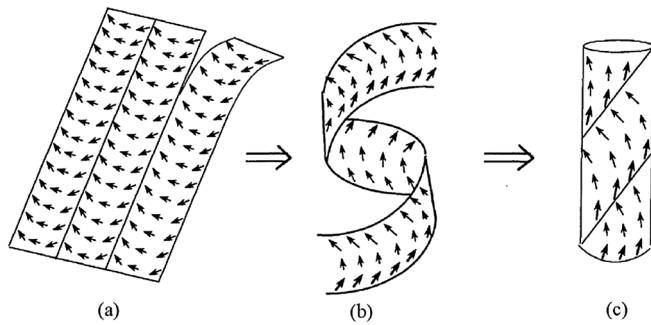


FIG. 12. Schematic illustration of the shape evolution of chiral bilayer membranes (a) with the molecules tilted with respect to their neighbors (indicated by the arrows) twisted into a helical ribbon (b) and a closed tubule when the lipid molecules are deposited from the saturated solution. From Ref. [128], reprinted with permission from AAAS.

differential growth [17,142], swelling and deswelling [11,15,23,143], and the coupling between piezoelectricity, electric polarization, and free charge-carrier distribution [144].

Strained multilayer structures receive intensive attention from the scientific community due to the applications as sensors and actuators in microelectromechanical and nanoelectromechanical systems. As mentioned earlier, the mechanical principles of residual stress or strain-induced bending of a multilayer can be exploited to manufacture micro- and nanoscale architectures. Prinz *et al.* [95] demonstrate that three-dimensional rolled-up nanohelices can be fabricated, through a top-down approach, by using an InAs/GaAs bilayer with lattice mismatch strain. The InAs layer is subjected to compression and the GaAs is in tension, because the lattice spacing of InAs is about 7.2% larger than GaAs. The bilayer rolls up (toward GaAs) to partially relax the interlayer strain due to mismatch, after the sacrificial layer (AlAs) is etched. This method relies on the fact that both layers are crystalline materials and grown epitaxially with respect to each other such that the lattice mismatch strain provides the driving force for bending. By controlling the geometric orientation of the strip, researchers can control the formation of rings or helices with preferred pitch angles (Fig. 13).

Since then, a variety of different crystalline materials have been used to manufacture bilayer or trilayer nanorings or nanohelices [10,138,145–147]. For instance, Bell *et al.* [145] manufacture three-dimensional InAs/GaAs nanosprings again by using AlAs as a sacrificial layer and employing a wet etch to release the patterned bilayers. Since crystallographic anisotropy dictates that the  $\langle 100 \rangle$  direction is the preferred roll-up direction, helical ribbons with different pitches and helix angles form depending on the misorientation angle of the ribbon's geometric axes and the bending direction (Fig. 13). This fabrication methodology takes advantage of the strain-engineering principle discussed above and achieves on-demand manufacturing of

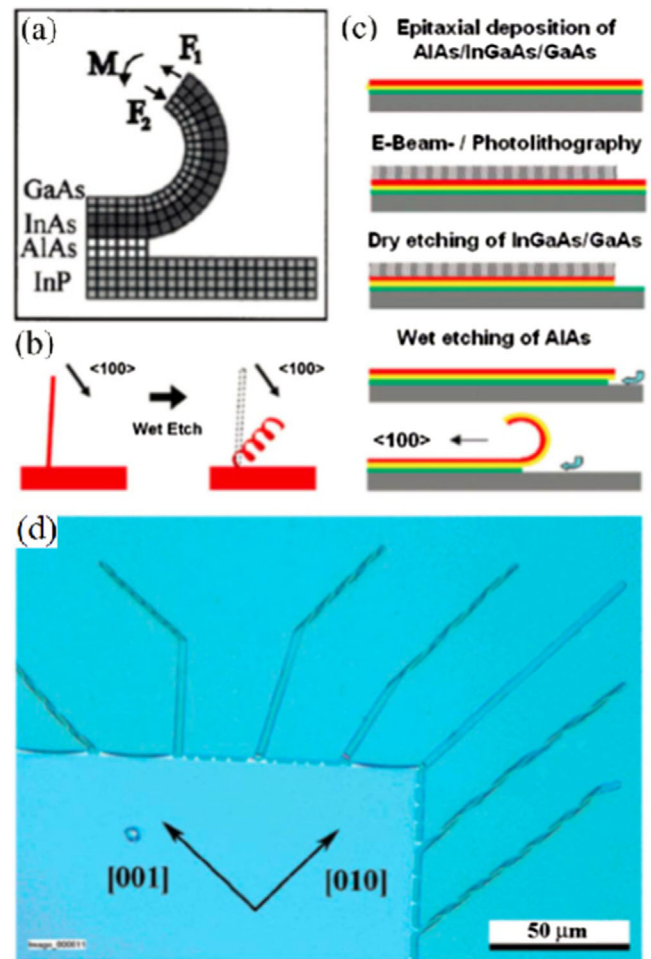


FIG. 13. (a) InGaAs/GaAs strain-induced curl; (b) releasing the strain generates helices; (c) bilayer fabrication; (d) helix pitch is a function of pattern orientation. Adapted with permission from Ref. [145] (© 2006 American Chemical Society).

semiconductor nanohelices with remarkable precision and reproducibility with potential applications as sensors and microrobotics.

Zhang *et al.* [10] further study the anomalous coiling phenomena in rolled-up SiGe/Si and SiGe/Si/Cr nanohelices. These nanohelices are manufactured by using the same methodology as described above. Interestingly, when the width is reduced from 1.3 to 0.7  $\mu\text{m}$ , the pitch and helix angle of the SiGe/Si/Cr helical nanohelix first decrease, then increase, and finally decrease until a self-overlapping ring forms. Noticeably, the chirality also switches from right-handed, to mixed, and to left-handed, suggesting that there could be some edge effects that influence the morphology. Indeed, Zhang *et al.* [10] take into consideration the edge effects by hypothesizing that the edge stress would become increasingly dominating when the width decreases, leading to the change of chirality, and the final self-overlapping state when the width falls below a threshold value (Fig. 14). Dai and Shen subsequently used a Cosserat rod theory to interpret this abnormal phenomenon

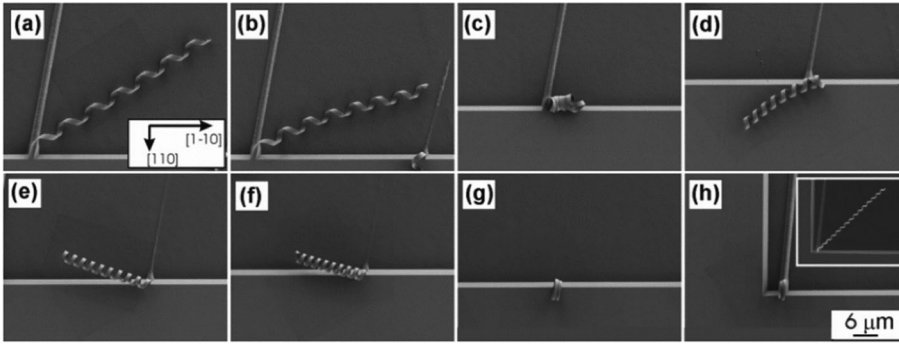


FIG. 14. SEM top view images of SiGe/Si/Cr helical nanoribbons (the layer thickness is 11/8/21 nm). The inset in (h) does not have a Cr layer. The arrows in (a) denote the  $\langle 110 \rangle$  direction on the substrate. All the strips in (a)–(g) have a misorientation angle of  $10^\circ$  from  $\langle 110 \rangle$ . The width decreases from  $1.30$  to  $0.70 \mu\text{m}$  at an interval of  $100 \text{ nm}$  from (a) to (h). In (h), both nanoribbons have a misorientation of  $5^\circ$ . Adapted with permission from Ref. [10] (© 2006 American Chemical Society).

by also considering the increasing edge effects as the width becomes larger [148].

### C. Mechanical self-assembly of helical ribbons: Modeling

More generally, a helical ribbon bends around two principal axes  $\mathbf{r}_1$  and  $\mathbf{r}_2$ , with principal curvatures  $\kappa_1$  and  $\kappa_2$ , as shown in Fig. 15(a). The principal bending axes form a misorientation angle  $\phi$  with the geometric axes  $\mathbf{d}_x$  and  $\mathbf{d}_y$ . Chen *et al.* [9] show that the coordinates of the center line can be parameterized as functions of the arclength  $s$ , and the geometric properties, such as the pitch  $p$ , the helix angle  $\theta$ , and the helix radius  $R$ , can all be determined by the three independent geometric parameters  $\kappa_1$ ,  $\kappa_2$ , and  $\phi$ :

$$p = 2\pi\tau/\alpha^2, \quad \theta = \sin^{-1}(\tau/\alpha), \quad R = \beta/\alpha^2, \quad (9)$$

where  $\alpha = \sqrt{\kappa_1^2 \cos^2 \phi + \kappa_2^2 \sin^2 \phi}$ ,  $\beta = \kappa_1 \cos^2 \phi + \kappa_2 \sin^2 \phi$ , and

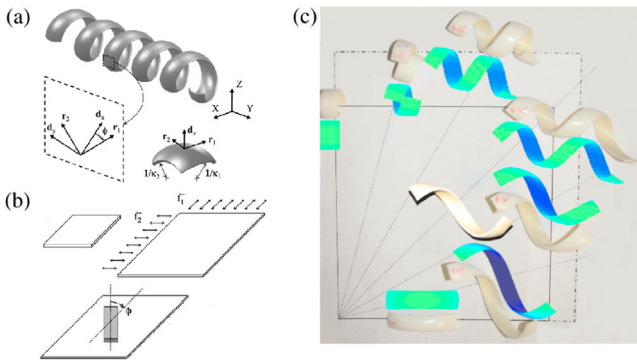


FIG. 15. Tunable helical ribbons. (a) Illustration of a helical ribbon. The principal bending directions,  $\mathbf{r}_1$  and  $\mathbf{r}_2$ , are rotated from the geometric axes,  $\mathbf{d}_x$  and  $\mathbf{d}_y$ , by a misorientation angle  $\phi$ . (b),(c) A piece of latex-rubber sheet is prestretched twice as much in the vertical direction than in the horizontal direction before a series of adhesive strips are attached to it along different misorientation angles ( $\phi = 0^\circ, 15^\circ, 30^\circ, 45^\circ, 60^\circ, 75^\circ$ , and  $90^\circ$ ). The ribbon at the center is made of prestretched top and bottom layers with a misorientation angle of  $30^\circ$ . The released multilayer strips deform into coiled shapes with the pitch and helix angle depending on  $\phi$ . Reprinted with permission from Ref. [9] (© 2011, AIP Publishing LLC).

$$\tau = (\kappa_1 - \kappa_2) \sin \phi \cos \phi. \quad (10)$$

Furthermore, they consider the deformation of a ribbon driven by surface stress ( $f^+$  and  $f^-$ ) acting on the top and bottom surfaces, respectively, by minimizing the total energy

$$\Pi = f^- : \gamma|_{z=-H/2} + f^+ : \gamma|_{z=H/2} + \int_{H/2}^{-H/2} \frac{1}{2} \gamma : C : \gamma dz, \quad (11)$$

where  $\gamma$  is the strain tensor,  $C$  is the elastic stiffness tensor, and the coordinate  $z$  is defined as the distance from the midplane along the thickness direction. Analytical solutions are then obtained for the case where  $f^+$  is zero. The theoretical predictions agree well with the tabletop experiments [shown in Fig. 15(b)], in which an elastic strip adhesive is bonded to a prestretched latex-rubber sheet to produce helical ribbons with different shapes depending on the misorientation angle ranging from  $0$  to  $90^\circ$  [Fig. 15(c)].

Armon *et al.* [15] also develop a theoretical framework to describe the formation of helical ribbons driven by incompatible target metrics and apply the model to interpret the chiral opening of *Bauhinia* seed pods [Fig. 16(a)]. The authors bond prestretched latex-rubber sheets to create a range of helical ribbon shapes. The predicted pitches and radii and the transitions between cylindrical helical ribbons and helicoids (which are discussed in detail in the next subsection) agree well with the resulting ribbon shapes. *Bauhinia* seed pods have been exploiting this mechanism to twist open into two pieces with opposite handedness for millions of years. Forterre and Dumais [149] further use paper models to illustrate the “phase space” of such helical ribbons. The fibers in their papers are typically aligned parallel to one side, so gluing two pieces of paper with perpendicularly aligned fibers forms an anisotropic bilayer. When immersed in water, this bilayer attempts to bend along both directions, creating saddle-shaped structures with a negative Gauss curvature. When the strips are cut along different directions, helical ribbons of different shapes form [Fig. 16(h)].

Since the theoretical approaches by Armon *et al.* [15] and Chen *et al.* [9] do not require the details of any microscopic interactions, the models can predict shape

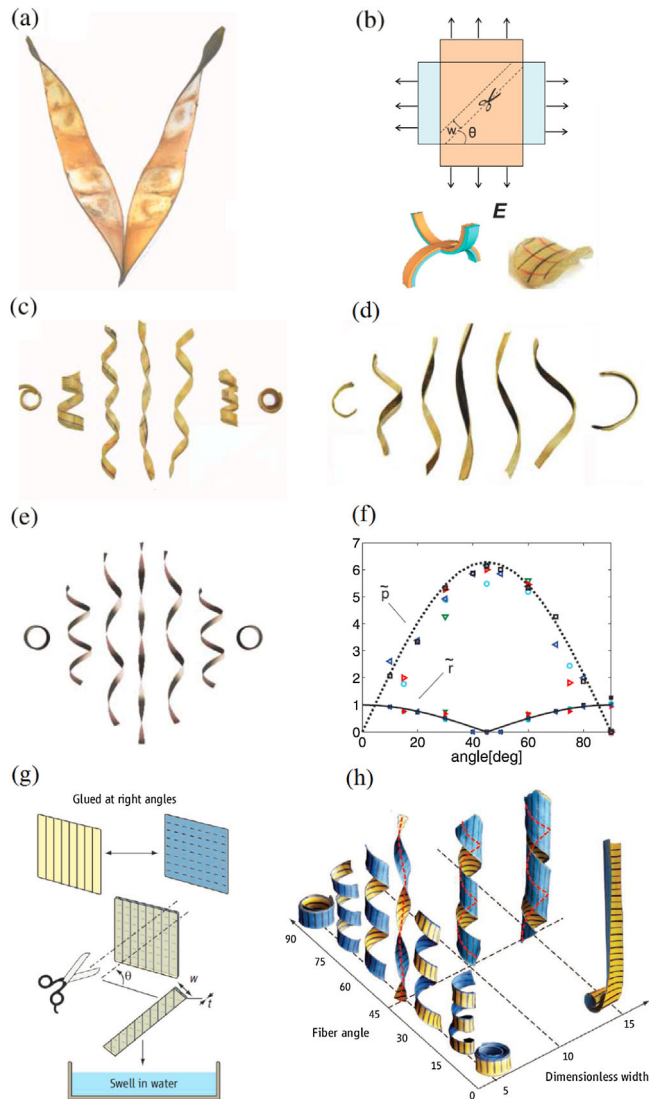


FIG. 16. (a) Open *Bauhinia* pods. (b) Manufacturing a mechanical analog of a *Bauhinia* pod. Bonding two perpendicularly prestretched latex-rubber sheets and gluing them together forms a residually stressed compound sheet. A strip is cut from the sheet along a direction that forms an angle  $\theta$  with either direction. (c)–(e) Narrow strips cut at angle  $\theta = 0^\circ, 15^\circ, 30^\circ, 45^\circ, 60^\circ, 75^\circ$  and  $90^\circ$  from a latex sheet, *Bauhinia* pods, and theoretical predictions, respectively. (f) Dependence of the radius and pitch on angle  $\theta$ . Symbols correspond to data points of the latex sheet, whereas lines are the theoretical predictions. (a)–(f) are from Ref. [15], reprinted with permission from AAAS. (g) The schematics for the method used to create paper models, which generates the coiling behavior that mimics plant structures. (h) The shapes of paper models for different combinations of the two control parameters: the dimensionless width and the misorientation angle. (g) and (h) are from Ref. [149], reprinted with permission from AAAS.

formation from any initially flat elastic sheet driven by residual stresses or strains, surface stresses, swelling or shrinkage, or differential growth [149].

Pham *et al.* [150] design and manufacture a class of stretchable nanoribbons able to transform into helices when

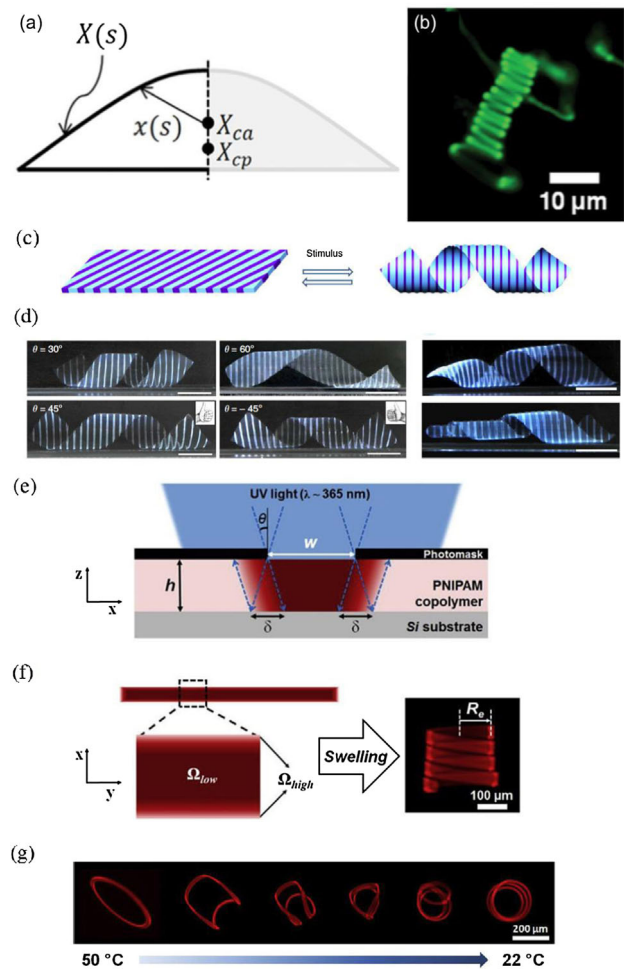


FIG. 17. (a) Theoretical cross section of isosceles nanoribbons, where  $X(s)$  is the path of the perimeter. The gray area is the imaginary mirror image. (b) Coiled nanoribbons immersed in water. (a) and (b) are adapted from Ref. [150] with permission (© 2013). (c) Left panel: A flat sheet made of the composite gel with 1-mm-wide patterned stripes of PNPAM gel (PG) and PNPAM/PAMPS gel (BG) that form an angle to the long axis of the sheet. Right panel: A helical ribbon formed when subjected to an external stimulus. (d) Helical ribbons generated after incubating the gel sheets for 24 h in a 1M NaCl solution. The right panels display conical helices generated in the NaCl solution by gradually changing the geometric parameters such as the ribbon width. (c) and (d) are reprinted by permission from Macmillan Publishers Ltd: Nature Communications, Ref. [151] (© 2013). (e) A 365-nm UV light is used to selectively cross-link a PNPAM copolymer sheet. The photomask restricts the regions of the sheet that are exposed to light, while the edges of the sheet under the edges of the photomask receive an intensity gradient of light, giving rise to a cross-linking gradient. (f) The swelling constant  $\Omega$  is low in the center of the ribbons, indicating that the centers have a limited capacity to swell. The edges are able to swell much more, resulting in a helix with defined radius  $R_e$  in a swollen state. (e)–(g) are reprinted from Ref. [152] (© 2014 with permission from Elsevier).

immersed in water. Ribbons are constructed from metal, polymer, and ceramic materials by using evaporative deposition. The nanoribbons have the cross section of an isosceles triangle, and this geometric asymmetry causes the

ribbons to spontaneously curl in an attempt to reduce energy [Fig. 17(a)]. The helices are formed only to the degree that they prevent the ribbon from self-intersection, leading to tight coils with low pitch [Fig. 17(b)]. Handedness is governed by the asymmetry of the cross section.

Helices are common in plant tendrils and have the tendency to reverse their chirality midway across their length. Godinho *et al.* study this perversion and create temperature-dependent cellulose liquid crystal fibers that mimic this effect [153]. Hydroxypropylcellulose is acetylated and crystallized and then electrospun into active micro- and nanofibers. These fibers wind upon heating while decreasing their tension. The authors also explore how the intrinsic curvature of the electrospun cellulose fibers is a product of fabrication and that the twist is due to off-core defects [154].

It is also worth mentioning that interfacial energy can also induce helical or even multiple-stranded helical shapes. Ji *et al.* [155] find that the interfacial adhesion could be responsible for the shaping of some double helices at the microscopic scale. Such double helices are observed in a variety of systems including DNA [156,157], carbon nanofibers [158], and carbon nanotubes [159,160].

## V. MECHANICAL PRINCIPLES OF SHAPE TRANSITIONS IN SELF-ASSEMBLED LAYERS

### A. Mechanical buckling induces formation of helical ribbons

While mechanical buckling has traditionally been perceived as a failure mechanism, in recent years researchers have employed buckling to construct a variety of geometric shapes including helices. Wu *et al.* [151] develop a new “small-scale,” modulation-based strategy to fabricate two-dimensional sheets that mechanically self-assemble into three-dimensional helical shapes. Inspired by the self-shaping of fibrous organs of plants, they develop stimuli-responsive single-layer composite materials that can undergo shape transformations. More specifically, they pattern a hydrogel sheet with stripes of alternating chemical compositions at a misorientation angle to the geometric axis of the ribbon. The difference in the swelling-deswelling ratios and elastic moduli between alternating stripes leads to a shape transformation of the 2D sheet into a helical ribbon, driven by a reduction in stretching energy. Remarkably, instead of having a residual strain or stress gradient (often through a multi-layer design), as is the case in previous works, the single layer in this study means that there is initially zero elastic modulus and stress or strain gradient along the thickness direction. In fact, the formation of helical ribbons here is due to mechanical buckling associated with the release of in-plane stretching energy, so the bending direction is always along the direction of the stripes. Cylindrical

helical ribbons with both right-handedness and left-handedness are generated with equal probability [Fig. 17(c)].

The buckling of thin hydrogel sheets is also shown to be controllable and reversible, paving the way for designing materials that respond naturally to their environment. Bae *et al.* [152] develop a simple manufacturing method to induce helical self-assembly when exposed to changes in temperature. Rather than changing the chemical composition of hydrogel sheets at different points, the researchers photo-cross-link the gel in such a way as to limit cross-linking on the edges of the ribbon [Figs. 17(e) and 17(f)]. The edges of the resulting ribbon are thus able to swell more than the center. Like the hydrogel ribbon developed by Wu *et al.* [151], the ribbon releases in-plane stretching energy by curling around a radius  $R_e$  (governed by the width of the ribbons). The curling of these ribbons is reliably reversible when the ambient temperature is increased to 50°. At these temperatures, the ribbons are less able to swell and the resulting in-plane stress between the edge and center is lower, reducing the curvature of bending. The authors posit that this behavior could have applications as a microknot that can be tightened or loosened in response to temperature. It should be noted that, unlike the periodically patterned hydrogel sheets in Wu *et al.* [151], a hydrogel ribbon that curls under edge effects alone has a natural pitch of 0—i.e., it has no off-axis bias and will naturally form a helix only to the extent that it prevents self-intersection [Fig. 17(b)]. A bias could theoretically be introduced by using the off-axis stripe techniques of Wu *et al.* [151], nevertheless. Interestingly, the authors find that the side of the ribbon exposed directly to UV light during photo-cross-linking reliably ends up as the inside of the curled ribbon. This is because the up-down orientation of the ribbon with respect to the light introduces a cross-linking gradient in the  $z$  direction. The side closer to the light cross-links more, making it less able to swell and pushing it to the inside of the curl.

While cross-linking-gradient edge effects serve as an extremely simple way to manufacture shape-morphing sheets, significantly more complicated structures can be built by selectively cross-linking the whole surface of a sheet. Kim *et al.* [161] use a “halftone lithography” approach to achieve arbitrary swelling and shrinking of sheets in two dimensions. They create an acrylic acid monomer solution with benzophenone photo-cross-linking units that gels proportionally to the amount of UV light received, allowing smooth variations in cross-linking levels. Rather than use difficult-to-produce grayscale photomasks, the authors opt to simulate gradations through the use of a halftone process, where the density of tiny circular regions of high UV is used to simulate varying levels of exposure [Fig. 18(a)]. This gives a wide range of possible cross-linking levels with only two binary photomasks. With this method, the authors first show that it is possible to easily produce common shapes that require only radially

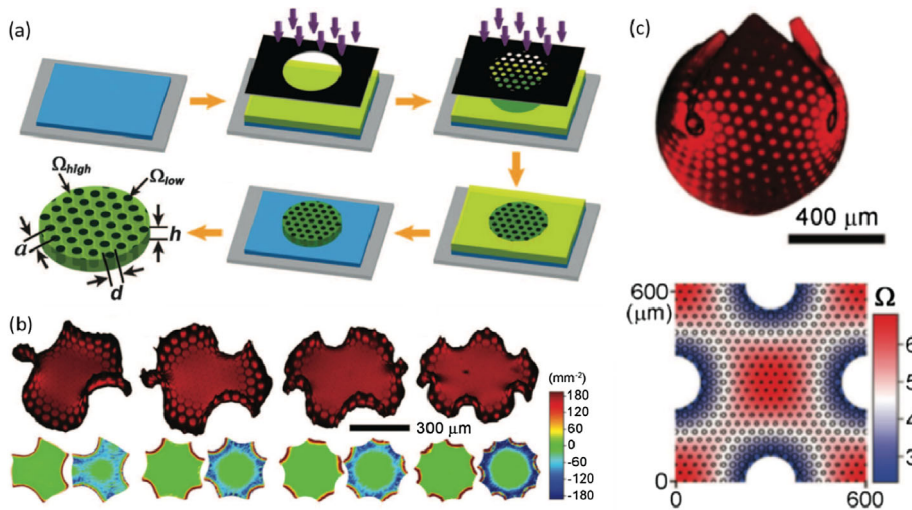


FIG. 18. (a) Flowchart showing the half-tone lithographic patterning method. A simple photomask is used to give the entire region a low dose of UV, and then a half-tone photomask gives selective high doses of UV. (b) Enneper's minimal surfaces generated from radially symmetric patterning. Surfaces with three to six nodes are generated. (c) Sphere generated from asymmetric patterning, with areas of high distortion excised. From Ref. [161], reprinted with permission from AAAS.

symmetric patterning such as saddles, cones, and Enneper's minimal surfaces [Fig. 18(b)]. These minimal surfaces are formed by mapping the swelling equation:

$$\Omega(r) = c \left[ 1 + \left( \frac{r}{R} \right)^{2(n-1)} \right]^2, \quad (12)$$

where  $n$  is the number of nodes and  $\Omega$  is the swelling ratio. It is found that the number of nodes on the resulting 3D shape could indeed be predictably varied, showing good agreement with the theory. More interesting shapes are possible with patterning that varies in two dimensions, such as a sphere. The authors take a conformal mapping of a square onto a sphere:  $\Omega(x, y) = 2(|dn(\alpha)sn(\alpha)|^2)/([1 + |cn(\alpha)|^2]^2)$ ,  $\alpha = (x + iy)/(R)(1/\sqrt{2})$ , where  $dn$ ,  $sn$ , and  $cn$  are Jacobi elliptic functions. This mapping has the advantage of concentrating distortion (which corresponds to extremely high or low levels of cross-linking) to a few small points, which could simply be excised from the sheet before swelling. The result [Fig. 18(c)] approximates a sphere, though the corners do not meet because of singularity effects.

There has been significant research into the development of PDMS-based adaptive bilayers that respond naturally to changes in environmental conditions, since PDMS's high biocompatibility makes it a promising candidate for drug delivery. Simpson *et al.* [162] show that, when plated with a dissimilar material, such as gold, the interfacial tension between the two materials causes controlled wrinkling. This wrinkling can be directed by locally modifying the thickness of either layer, leading to the creation of complex structures. The bilayers that they create are able to coil and uncoil in response to temperature changes, allowing them to capture and release poly(ethylene glycol). In a similar study, Kalaitzidou and Crosby [163] show that it is possible to create adaptive polymer bilayer particles that undergo shape actuation when exposed to interfacial stress. These small particles change the characteristics of the fluid flows

they are in based on whether they are in a rolled or unrolled state. Sheets of PDMS are cured and plated with a gold layer through *e*-beam evaporation. These sheets are then cut into pieces with set lengths and widths, which determines their subsequent shape transformation. They find that, when both dimensions are significantly larger than the PDMS sheet thickness, the particles tend to roll into tubes and rings. As the thickness increases, the particles roll into open structures such as arcs and helices [Figs. 19(a) and 19(b)]. This process is shown to be reversible, with the coils and tubes returning to a two-dimensional state upon a sufficient temperature increase. They show that the small size of the coils allows them to be used as adaptive particles in a solution to control the flow of that solution based on the temperature. This is generalizable to a large number of responsive polymers and environmental stimuli.

Agrawal *et al.* [164] show that uniformly aligned liquid-crystal (LC) elastomers could be made to actuate in complex shapes by affixing a secondary polystyrene layer

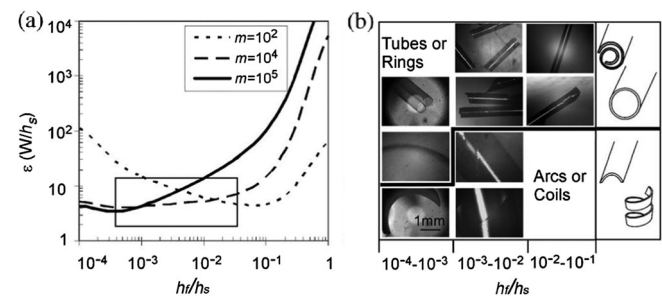


FIG. 19. (a) Phase diagram showing the cutoff point for when polymer bilayer particles will form complete tubes and rings (above lines) versus arcs and coils (below lines). The  $x$  axis is the ratio of layer thicknesses, the  $y$  axis is the radius of curvature, and each line corresponds to a different biaxial modulus. (b) Examples of structure found above and below the lines. (a) and (b) are reprinted with permission from Ref. [162] (© 2008, AIP Publishing LLC).

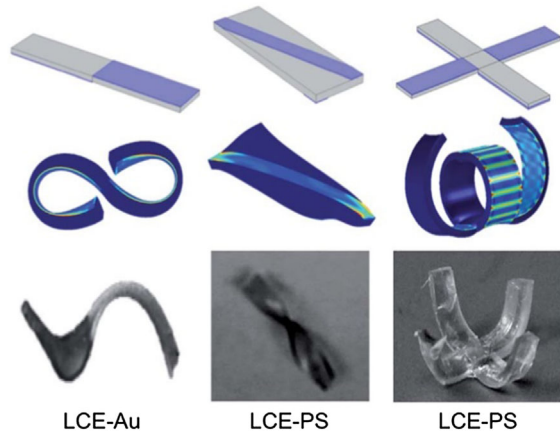


FIG. 20. Various structures formed by LC elastomers adhered to a polystyrene layer. Bends, folds, and twists are introduced, as well as a four-arm grabbing structure. Reproduced (adapted) from Ref. [164] with permission of The Royal Society of Chemistry.

that locally varies in thickness. When heated, the LC elastomer attempts to contract along its alignment director but is inhibited by the polystyrene layer. In regions of thin polystyrene the balancing of deformation energy causes small wrinkles, but as the polystyrene becomes thicker, the wavelength and amplitude of the wrinkles increase until the sheet folds. The authors show that applying polystyrene films on opposite layers can make further complex shapes. A four-arm grabbing actuator is made by selectively patterning the arms of a cross (Fig. 20). The polystyrene is placed on top of the LC, where the alignment director is parallel to the direction of the intended bend, while it is placed under the LC with perpendicular alignment. When heated, both sets of arms curl upward in a grasping motion. This pattern can be extended to a planar LC elastomer-polystyrene bilayer, which results in an actuator that functions like a leaf-closing when the temperature rises too high and opening when it falls.

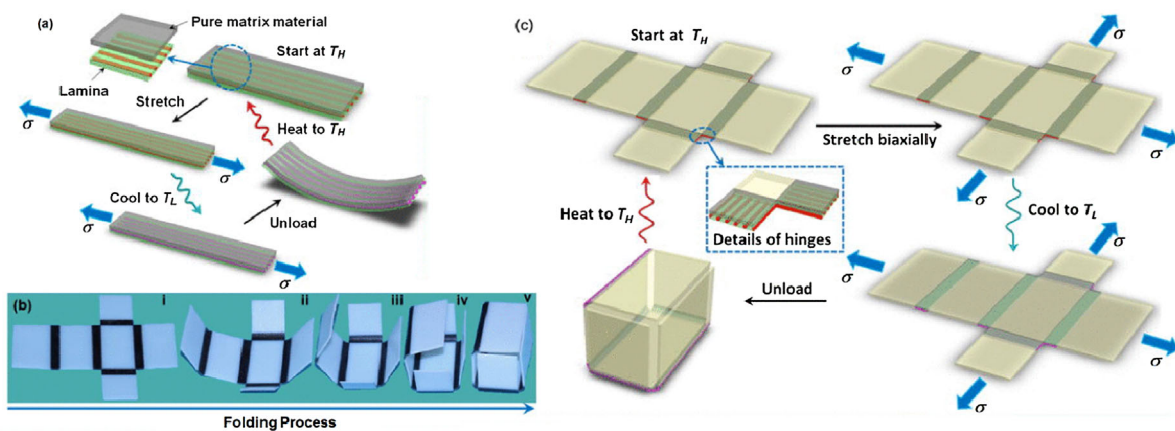


FIG. 21. (a) Thermal cycle of shape memory fiber-embedded elastomers. When stretched and cooled below the glass transition temperature of fibers, the composite bends on unloading. When reheated, it returns to a flat state. (b),(c) Self-folding box made from this technique, where the fibers are embedded in the folds. Reprinted with permission from Ref. [5] (© 2013, AIP Publishing LLC).

Shape memory alloys have long been a promising material in the field of shape-morphable structures but have been hindered by their lack of flexibility. Recent advances are helping to remove this barrier, such as the work of Ge *et al.* [165], who design a composite structure where shape-memory fibers are embedded in an elastomer matrix [165]. This allows them to encode shape-morphing behavior into the fibers. Using a multimaterial 3D printer, glassy shape-memory fibers with preprogrammed shape effects are printed into the elastic matrix. When the resulting material is stretched and cooled below the glass transition temperature of the fibers, it curls when the stretching force is released. When heated to above the glass transition temperature, the material recovers its original shape [Fig. 21(a)]. The authors use this property to design and print a self-folding box, in which each of the hinges is composed of this curling design. The box is stretched and cooled and upon release folds itself. When reheated, it similarly unfolds [Figs. 21(b) and 21(c)].

Xu *et al.* [166] show that it is possible to induce buckling-driven self-assembly of helical ribbons in almost arbitrary materials. Winding silicon ribbons are placed on a prestretched elastomer. Using UV light to generate ozone at specific points on the surface of the ribbon induces the formation of hydroxyl groups, which allows the ribbon to bind to the prestretched elastomer at well-defined points. When the elastomer is allowed to relax, the ribbons deform out of plane in order to minimize internal stress [Fig. 22(a)]. In this case, the radius of the resulting helix, as well as the pitch and chirality, is all determined by the spacing of the bonding hydroxyl groups in relation to the ribbon. Unlike the helices made of hydrogels in Bae *et al.*'s work [152], these helices once formed are permanent. The authors also find that by using finite-element analysis to precompute the strain on the ribbons they are able to manufacture multi-layer architectures. The higher layer strips of silicon, rather than buckling around hydroxyl bonding sites, buckle

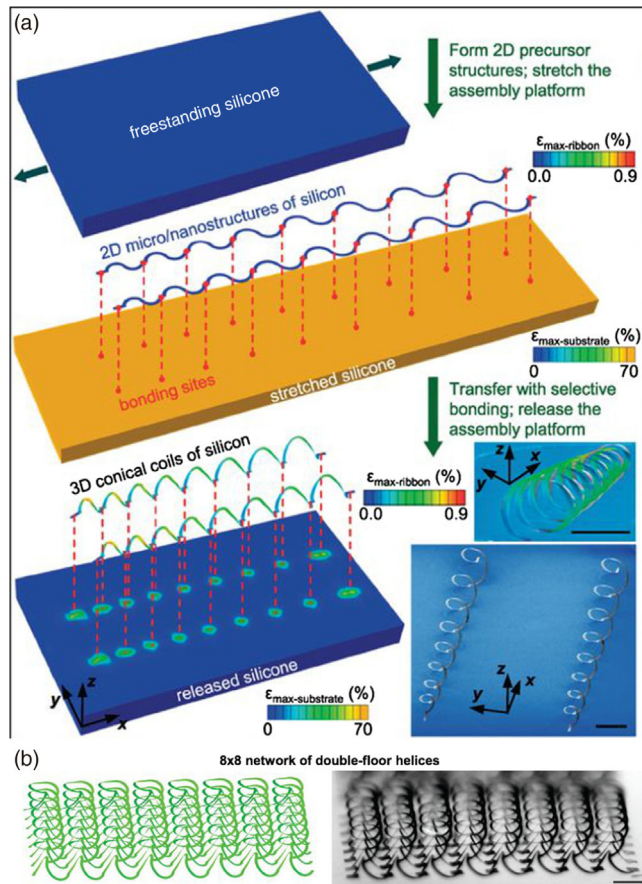


FIG. 22. (a) Nanohelix structure formed from wavy silicon ribbon selectively bonded to an elastomer sheet. (b) A similar technique is used to make double-helix structures, where the second layer of helices stands on top of the first. This second layer is not bonded to the elastomer. From Ref. [166], reprinted with permission from AAAS.

around their joins to other silicon strips, enabling the formation of double-layered helices [Fig. 22(b)]. This technique is very promising primarily because of the impressive maturity of silicon lithography technology. Since the deformations rely on the same techniques that are used to pattern silicon chips, 3D out-of-plane nanostructures can be made at an extremely high resolution. The authors show that this technique is also extensible to metals and other semiconductors, indicating impressive versatility.

### B. Shape transitions in helical ribbons

Recent studies show that shape transitions can occur between purely twisted ribbons, helicoids, spiral ribbons, and tubules by changing the relevant geometric parameters, such as the magnitudes and signs of the principal curvatures, the misorientation angle, or the geometric dimensions [9,15,21–23]. These changes often result from external stimuli, such as changes in the temperature [24,167], pH, or swelling and deswelling [15,23].

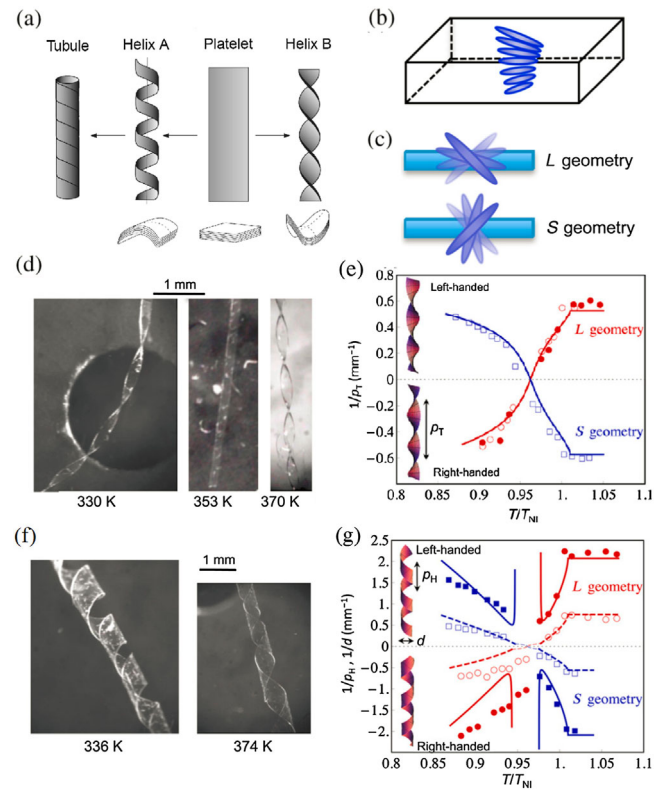


FIG. 23. (a) Schematic representation of cylindrical helical and purely twisted ribbons. The bottom shapes feature the locally cylindrical and saddlelike curvatures in these multilayered ribbons. Adapted from Ref. [127] with permission. (b) Side view of schematics of the direction of twisted-nematic-elastomer (TNE) ribbons. (c) A schematic diagram shows the top view of  $L$  and  $S$  geometry. (d) Micrographs of cylindrical helical ribbons formed by the wide TNE where the thickness of the ribbons is  $35.2 \mu\text{m}$ . The  $L$ -geometry ribbon is left-handed at  $374 \text{ K}$  and right-handed at  $336 \text{ K}$ . Reprinted with permission from Macmillan Publishers Ltd: Nature, Ref. [127] (© 1999).

Oda *et al.* [127] study the transition between helicoids and spiral ribbons in charged gemini surfactants when the length of the molecular chain changes [Fig. 23(a)]. These shape transitions are also observed in twist-nematic elastomers [1,24]. Sawa *et al.* [24] find that thin ribbons undergo a similar transition when the width varies and develop a theoretical model by introducing a term in the total potential energy that accounts for molecular twist. Twist-nematic-elastomer ribbons can form purely twisted or cylindrical helical shapes depending on the temperature and/or width. This shape selection arises from the competition between the bending energy and in-plane stretching energy. A ribbon with a small width-to-thickness ratio can easily adopt a twisted shape with a large Gauss curvature; while one with a large width-to-thickness ratio

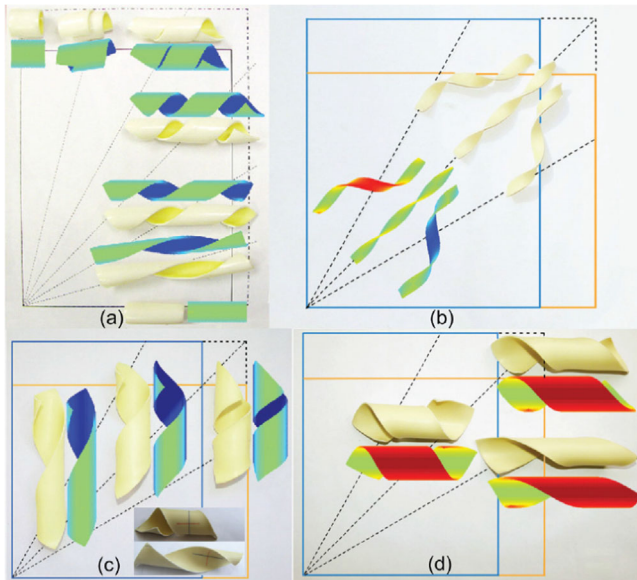


FIG. 24. Monostable and bistable helices. (a) Monostable helical ribbons. An elastic strip is bonded to a prestretched latex-rubber sheet, with a misorientation angle  $\phi$  ranging from 0 to 90° at a 30° interval. The prestretches are 0.24 and 0.12 in the vertical and horizontal directions, respectively. (b) Monostable helical ribbons. (c) Bistable helical ribbons. (d) The other stable shapes of the same ribbons in (c). The color is indexed according to the out-of-plane displacement. Reprinted with permission from Ref. [22] (© 2014, AIP Publishing LLC).

will stay in a shape with nearly zero Gauss curvature to minimize the total potential energy (and, in particular, the stretching energy). The change in temperature, on the other hand, results in local stretches (or shrinks) along the nematic director caused by residual effects from temporary chiral dopants. They also show that certain liquid-crystal elastomer ribbons could switch chirality when transitioning with changes in temperature.

Armon *et al.* [15,23] and Guo *et al.* [22] independently examine shape transitions in strain-engineered elastic ribbons and come up with similar criteria that a transition would occur at when the dimensionless “width”  $W/\sqrt{\kappa/H}$  (where  $W$  is the width,  $H$  is the thickness, and  $\kappa$  is the principal curvature) exceeds the threshold value. So the transition in shape (as well as multistability, as discussed later) is actually dictated by the combination of these three geometric parameters. Guo *et al.* [22] further perform theoretical analysis and experiments (Fig. 24) to study such shape transitions and the associated change in multistability. Finite-element simulations (Fig. 25) are also employed to quantitatively investigate such shape transitions [168]. (In fact, these shape transitions occur not only in surfactants, strained elastic ribbons, and liquid-crystal elastomers, but also in seed pods and peptides related to Alzheimer’s diseases.)

Among the key parameters that control the shape of the deformed ribbon are the misfit strains, the misorientation angle, the width, the thickness, and the elastic layer

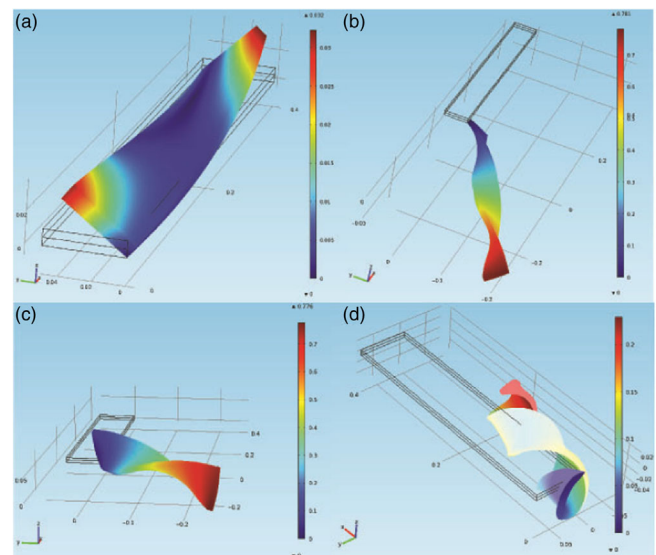


FIG. 25. The stable helical configurations driven by misfit strains in bilayer ribbons modeled using finite-element simulations. The misfit strain in the top layer is  $\underline{\underline{\epsilon}}^0 = (\epsilon_1 \cos^2 \phi + \epsilon_2 \sin^2 \phi) \underline{e}_1 \otimes \underline{e}_1 + (\epsilon_1 \sin^2 \phi + \epsilon_2 \cos^2 \phi) \underline{e}_2 \otimes \underline{e}_2 + (\epsilon_1 + \epsilon_2) \sin \phi \cos \phi (\underline{e}_1 \otimes \underline{e}_2 + \underline{e}_2 \otimes \underline{e}_1)$ , where (a)  $\epsilon_1 = 0.02$ ,  $\epsilon_2 = -0.02$ ,  $\phi = \pi/4$ ,  $L = 0.4$  m, and  $W = 0.04$  m; (b)  $\epsilon_1 = 0.1$ ,  $\epsilon_2 = -0.1$ ,  $\phi = \pi/4$ , and  $W = 0.04$  m; (c)  $\epsilon_1 = 0.1$ ,  $\epsilon_2 = -0.1$ ,  $\phi = \pi/4$ ,  $L = 0.4$  m, and  $W = 0.08$  m; and (d)  $\epsilon_1 = 0.5$ ,  $\epsilon_2 = -0.5$ ,  $\phi = \pi/4$ ,  $L = 0.4$  m, and  $W = 0.08$  m. Transition from a purely twisted ribbon (c) to a spiral ribbon (d) occurs when the misfit strain is increased by 5 times. The color (in this figure and the following) is indexed according to the total displacement to help visualize the deformation involved. With kind permission from Springer Science+Business Media, Ref. [168] (© 2014).

properties. Notably, a purely twisted ribbon forms [Figs. 24(b) and 25(b)] when the principal misfit strains are such that

$$\epsilon_1 \cos^2 \phi + \epsilon_2 \sin^2 \phi = 0. \quad (13)$$

This result agrees well with the previous study by Chen *et al.* [9]; namely, a purely twisted ribbon forms if and only if  $\kappa_1 \cos^2 \phi + \kappa_2 \sin^2 \phi = 0$  (where  $\kappa_1$  and  $\kappa_2$  are the principal curvatures).

It is worth pointing out the differences between a helicoid and a purely twisted ribbon, which can be confusing at times [169]. A helicoid is the only ruled minimal surface besides a plane. In fact, the center line of a helicoid ribbon does not necessarily have to be straight but can also be a helix. In comparison, a purely twisted ribbon has a straight center line, and the radius of the bounding cylinder is zero. Mathematically, a helicoid has principal curvatures  $\kappa_1$  and  $\kappa_2$  such that  $\kappa_1 + \kappa_2 = 0$ . Therefore, a purely twisted ribbon becomes a helicoid when  $\kappa_1 = -\kappa_2$  and  $\phi = \pi/4$ .

Cranford and Buehler [170] develop a multiscale molecular-dynamics approach by adopting a two-dimensional coarse-grained model to recapitulate the

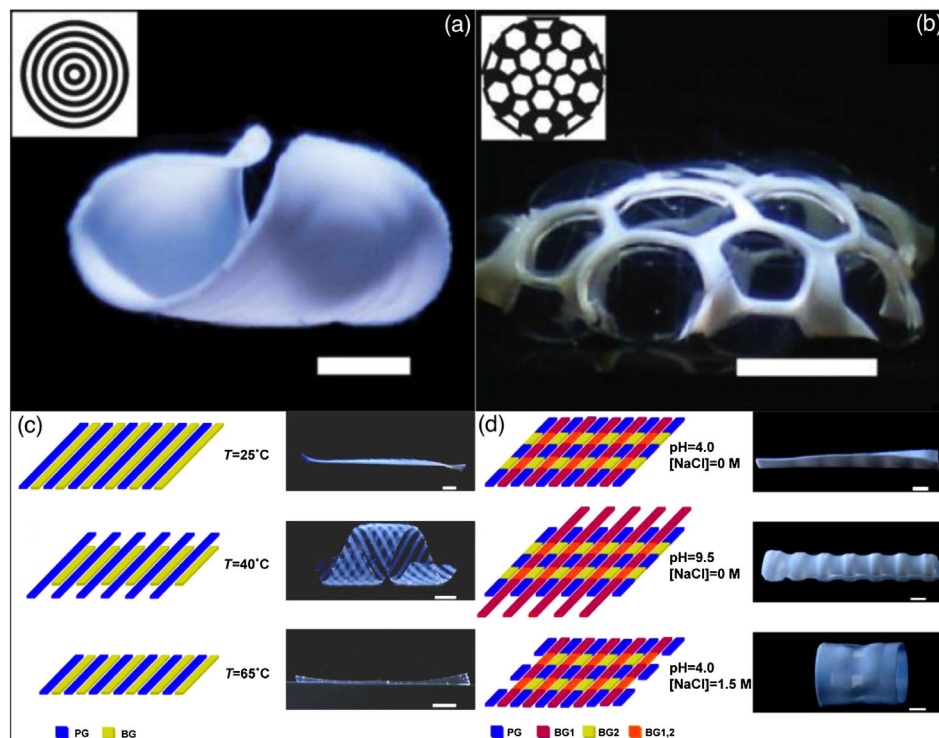


FIG. 26. (a) Saddle-shape structure formed from concentric ring-patterned sheet. (b) Icosahedron formed from projection-patterned sheet. (c) Multistage material that coils upon reaching  $40^\circ$  and uncoils upon reaching  $65^\circ$ . (d) Multistimulus material that curls into a long thin tube under high pH and a short fat tube under high salinity. Adapted with permission from Ref. [173] (© 2013 American Chemical Society).

mechanical self-assembly of mono- and multilayer graphenes. A spontaneous transition from a purely twisted configuration (helicoid) to a coiled shape in graphene ribbons is identified, which gives rise to a strain filled with more homogeneity. The results are similar (but not identical) to the experimental observations and theoretical predictions by Armon *et al.* [15,23] and Guo *et al.* [22], as well as the results by Lee *et al.* [171], Kit *et al.* [172], and Chen *et al.* [137], but, in the work by Cranford and Buehler, the transition to the coiled shape is mainly because of a mechanical instability “between the imposed strain of the twisted graphene ribbons and the bending stiffness” [170]. As a result, this transition occurs more frequently in stiffer or thicker graphene ribbons.

Recently, Wu *et al.* [151] demonstrated the possibility of achieving multiple programmed shape transformations between different geometric shapes under ambient conditions by integrating multiple, small-scale modulated structural components within planar sheets. Continuous, reversible shape transformations in response to external thermal or chemical stimuli, from planar sheets to three-dimensional arcs, to helices, and tubules, are fulfilled by this design strategy which exploits mechanical buckling principles. This approach can be readily extended to other materials such as elastomers and liquid-crystalline polymers to enable functionality that can be coupled with shape transitions.

Therien-Aubin *et al.* [173] develop a hydrogel able to go through multiple shape transformations in response to a wide range of stimuli, including temperature, pH, ionic strength, and  $\text{CO}_2$ . These gels also respond differently to

various stimuli. They first show that a sheet treated with poly(*N*-isopropylamide) and patterned with a truncated icosahedron assumes the shape of an icosahedron when exposed to a NaCl solution. By using a different chemical treatment, they are able to force a sheet printed with circles of chemicals to adopt a saddle shape when exposed to  $\text{CO}_2$  [Fig. 26(a)], and an icosahedron-patterned sheet to adopt a similar structure [Fig. 26(b)]. These transformations are reversible and show resilience to hysteresis. The authors then pattern a hydrogel ribbon to respond to heat: As it is heated above ambient temperature, it curls into a helix, but when heated above the lower critical solution temperature of the doping chemical, it returns to a flattened state [Fig. 26(c)]. Finally, a hydrogel sheet is manufactured that responds to both pH and ionic concentration. The sheet is patterned with stripes along the width that activate under changes in pH, while stripes along the length move in response to changes in ambient ionic concentration. This results in a gel that is able to assume a gradient of shapes based on the relative strengths of the two stimuli: When exposed to high pH alone, the sheet rolls into a tight long cylinder, and when exposed to high ionic concentrations alone, the sheet rolls into a wide compressed cylinder [Fig. 26(d)].

Furthermore, the chemical-mechanical coupling in these model systems may advance the current understanding of the deformation and actuation of fibrous living organs [151]. In particular, Iamsaard *et al.* [174] show that helical ribbons constructed from liquid-crystal polymer networks could be designed to mimic the response of plant tendrils unfolding [Figs. 27(a)–27(f)]. Current research indicates

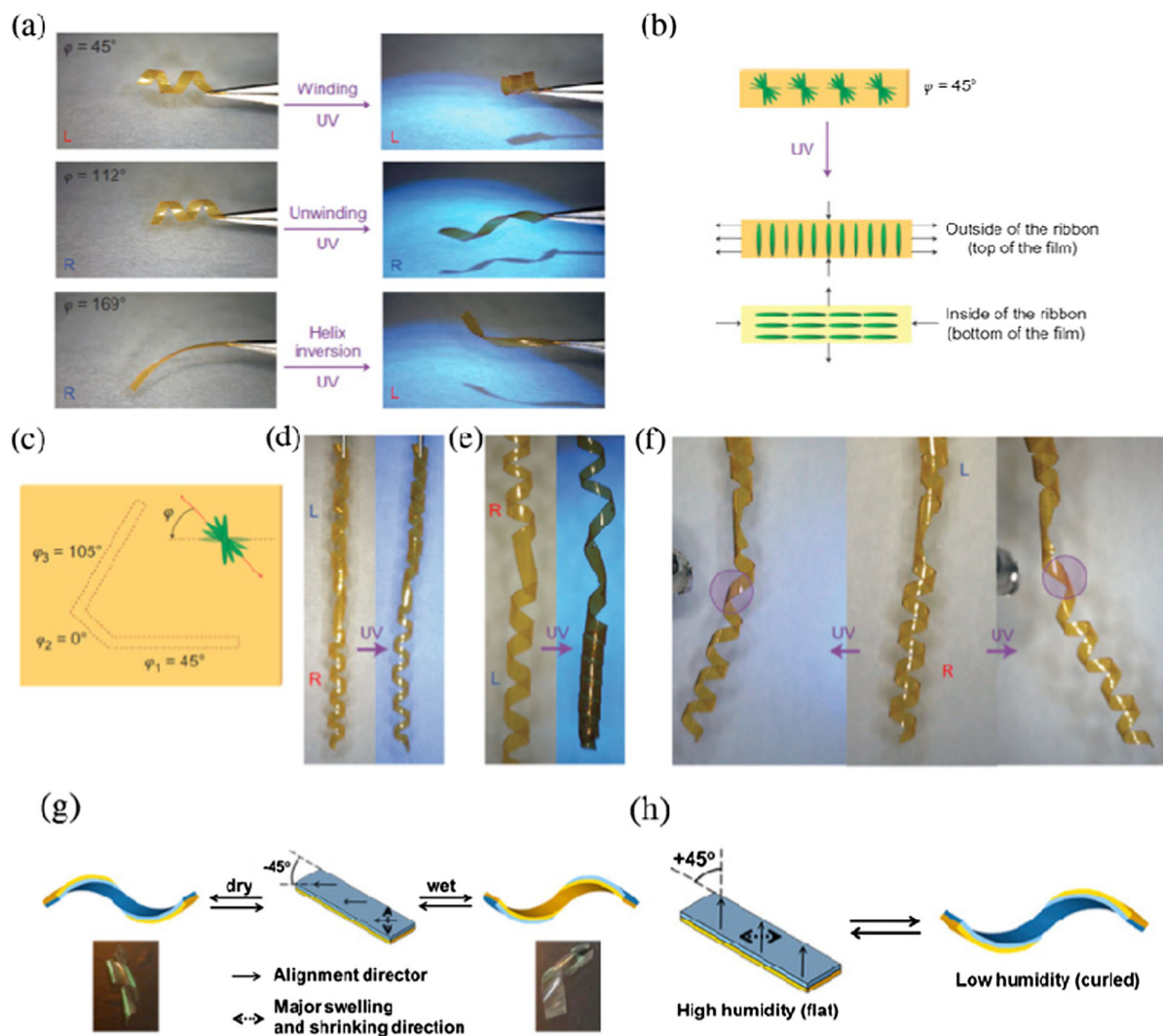


FIG. 27. (a),(b) LC helix curling, uncurling, and inversion under UV light exposure. Helices where the handedness is reinforced by the alignment director will curl when exposed to UV light, but those where handedness is opposite to alignment director will uncurl and eventually invert. (c)–(f) When selectively irradiated by UV light near the kink, the end of the helical ribbon constructed from liquid-crystal polymer moves away and off axis from the other end. Reprinted with permission from Macmillan Publishers Ltd: Nature Chemistry, Ref. [174] (© 2014). (g),(h) Diagram showing how alignment director of the initial LC network informs the handedness of the resulting helix. (g) and (h) are adapted with permission from Ref. [175] (© 2014 American Chemical Society).

that the elongation of rectangular plant cells in one direction and shrinking of the cells in the transverse directions to cause tendril unwinding is very similar to the shape change of liquid crystals under stimulation [153]. The authors attach a helical coil with right-hand chirality to a coil with left-hand chirality, joined at a kink (the equivalent to a tendril perversion in plants). When selectively irradiated near the kink by UV light, the side belonging to the right-handed helix coiled further, while the side belonging to the left-handed helix uncoiled [Fig. 27(f)]. This behavior causes the end of the synthetic tendril to move both away and off axis from the other end, as the kink becomes a joint where macroscopic bending can take place.

Liquid-crystal polymer networks have also been made to actuate in response to changes in humidity. de Haan *et al.*

[175] construct a LC polymer sheet that could undergo bending and twisting when stimulated by uniform humidity [Figs. 27(g) and 27(h)]. After dipping in KOH and rinsing in water, the sheet bends towards the untreated side, but when dried, it bends towards the other side [Fig. 27(f)]. The authors treat the sheets with a basic solution in specific patterns and observe the resulting shape change in humidity. A ribbon treated with an alternating pattern assumes an accordion shape in low humidity, while a ribbon with narrow treated bands forms a sharp hinge. They then cut a ribbon with an alignment  $45^\circ$  off center and show that it curls right-handed around an axis in the dry state and becomes straight in high humidity, forming helices [Fig. 27(g)].

Plant shape change, on the other hand, is generally driven by uniform changes in environmental conditions, such as

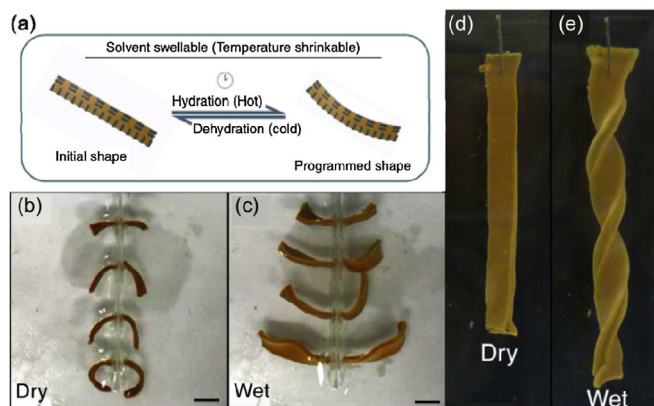


FIG. 28. (a) Diagram showing programmed shape transition under hydration. (b),(c) Dry and wet states of uniform curling and uncurling composites. (d),(e) Dry and wet states of twisting composites. Reprinted with permission from Macmillan Publishers Ltd: Nature Communications, Ref. [176] (© 2013).

humidity. Thus, any asymmetric shape change must be encoded in the plant's internal heterogeneous structure, usually through the judicious placement of stiff cellulose microfibrils (CMFs) that respond differently to humidity than the surrounding tissue. Erb *et al.* [176] develop a framework for manufacturing synthetic shape-change composites based on this natural design. The authors investigate the reinforcement architecture seen in seed dispersal units that bend and twist. Aluminum oxide platelets electrostatically bonded to superparamagnetic iron oxide nanoparticles are used to simulate the effect of CMFs while also allowing the orientation of the platelets to be controlled by weak external magnetic fields. These platelets are mixed into fluid polymer solutions to produce bulk hygroscopic composites, and the resulting solutions are gelled in the presence of magnetic fields. Composites that bend are produced by using a bilayer configuration to mimic pinecone architecture, in which the first layer is deposited under the influence of a uniform magnetic field and the second from a rotated uniform field [Fig. 28(a)]. When the resulting composite is dried, it bends towards the layer with the platelets oriented perpendicular to the long axis [Figs. 28(b) and 28(c)]. A similar system that twists like a seed dispersal unit is built by changing the bending bilayer configuration to have all the platelets also off axis by  $45^\circ$ . This causes the layers to attempt to expand in directions perpendicular to one another and results in a twist [Figs. 28(d) and 28(e)]. Both the bending and twisting systems could be brought back to a flat state through drying. Multiresponsive composites are also obtained that respond to both hydration and heat. Hydrogel with alumina platelets in the twisting bilayer configuration twists to the right when heated as the gel loses its ability to store water. When hydrated over a long period of time, the composite twists with the opposite chirality.

Many of the physical systems mentioned above are inspired by biological phenomena. In turn, systematic

studies on the chemical-mechanical coupling in these model systems may advance the current understanding of the deformation and actuation of fibrous living organs [151].

### C. Change of handedness

While many of the helical structures have a uniform chirality or handedness (i.e., are either left-handed or right-handed), a change of handedness can occur under certain circumstances. For example, growing plant tendrils are found to switch handedness after the two ends are fixed in space; the tendrils develop coexisting left-handed and right-handed parts connected by perversions [Figs. 29(a) and 29(b)] [11,177,178]. Inspired by these tendril perversions, Huang *et al.* [12] bond two elastomer strips of unequal length, one of which is prestretched, to create hemihelices and perform finite-element simulations to interpret their findings. Savin *et al.* [17] also construct hemihelical structures to mimic the looping guts in developing embryos. They prestretch a rubber sheet and stitch to it a rubber tube along the side [Fig. 30(a)]. When relaxed, the tube develops a pattern featuring multiple hemihelical segments connected by perversions [Fig. 30(b)], resembling the shape of chick guts [Fig. 30(c)].

Gerbode *et al.* [11] construct bilayer silicone ribbons, one layer of which is prestretched, to study the physical mechanisms of the coiling and overwinding of the cucumber tendrils. Again, the topological constraint from the two fixed ends dictates that perversions form, but the perversions that connect the helical segments of opposite handedness also allow for rotations, causing an increase in the number of helical turns. Their study shows that when bending stiffness is smaller than twisting stiffness, the ribbon unwinds upon extension. However, for a helix with a round cross section, the bending stiffness is always larger than the twisting stiffness, which indicates that overwinding occurs upon extension. As a result, the "twistless springs" can undergo axial extension simply through overwinding without paying an additional energy penalty for changing the curvature, a good strategy for creating soft springy tendrils that stiffen upon further deformation [11].

Liu *et al.* [179] further investigate the transitions between a helix and a hemihelical structure (with perversions). It is found that the twist buckling instability could prevent the system from going to the lowest energy state. These buckling modes lead to the formation of hemihelices that include multiple perversions but have higher energy than a simple helix. The system, once trapped in the metastable state, would have to be deformed by external forces and torques in order to return to the global energy-minimum state. The researchers use a combination of experiments, finite-element simulations, and theoretical analysis (based on Kirchhoff's rod theory) to demonstrate that the aspect ratio, which is closely related to the ratio between the bending stiffness and twisting stiffness, plays a

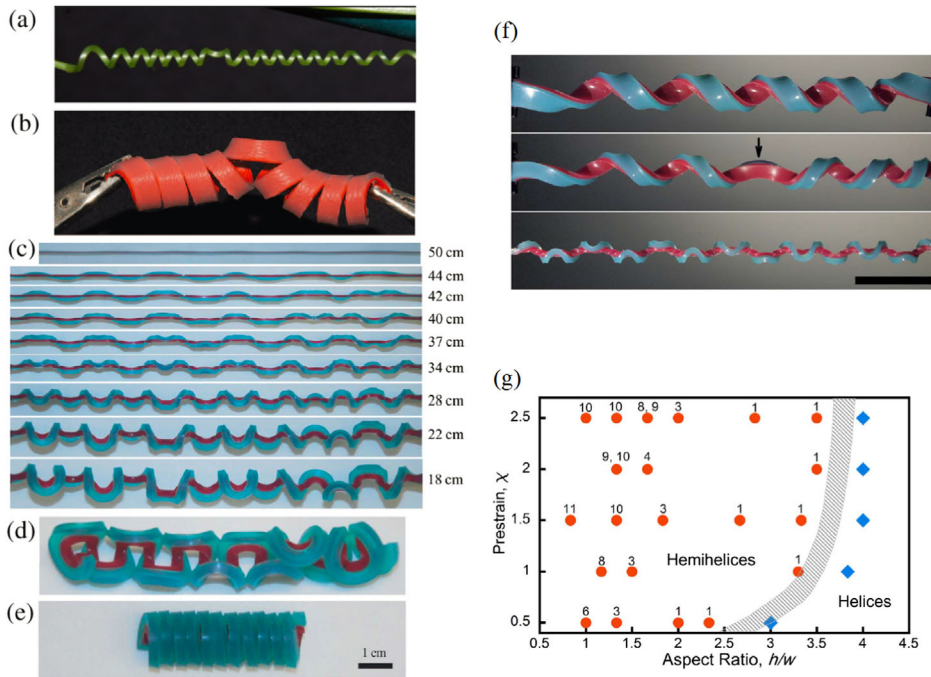


FIG. 29. (a) Fiber ribbon that overwinds around the perversion when pulled. (b) Twistless spring with low bending stiffness and high twisting stiffness that unwinds when pulled. From Ref. [11], reprinted with permission from AAAS. (c)–(e) are adapted from Ref. [12] with permission of The Royal Society of Chemistry. (f) Helices with decreasing cross-section height-to-width ratio. The structure moves from helix, to hemihelix, to hemihelix with multiple perversions. (g) Number of perversions as function of aspect ratio and prestrain. Adapted from Ref. [179] with permission.

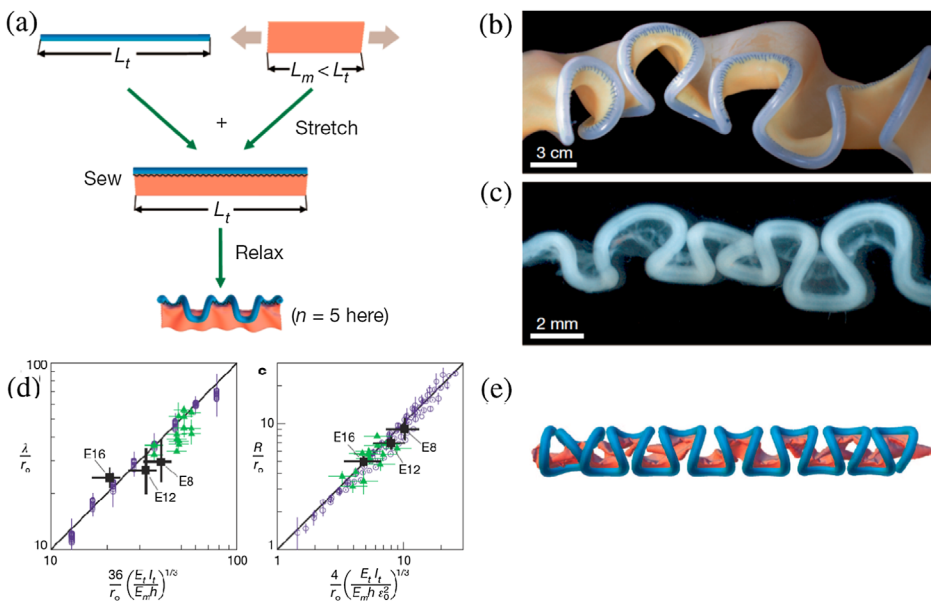


FIG. 30. (a)–(c) Thin stretched rubber sheets are stitched to unstretched rubber tubes to induce twisted patterns that resemble the looping guts in chick embryos in (c). (d), (e) Scaling laws for the loop shape, size, and number at three stages in the development of chick guts. Reprinted with permission from Macmillan Publishers Ltd: Nature, Ref. [17] (© 2011).

key role in determining the number of perversions per unit length.

Yet another way of fabricating a helical ribbon with both left-handed and right-handed parts is by virtue of a V-shaped mesa design [Figs. 31(a)–31(c)] [138,146]. For example, Fig. 31 shows that such a structure can be achieved by designing a mesa shape where  $2\alpha + \theta_1 + \theta_2 = 270^\circ$ . In order for the left- and right-handed helical segments to be symmetric, it should follow that  $\theta_1 = \theta_2$ . In Fig. 25(b), it is set that  $\theta_1 = \theta_2 = 75^\circ$  and  $\alpha = 60^\circ$ .

In all the cases discussed above, the changes in handedness occur when the ribbon has two fixed ends. However,

such geometric constraint is not a necessary condition for a switch in handedness. It is found that in SiGe/Si/Cr nanobelts left-handed and right-handed segments could coexist when the misalignment angle is slightly larger than  $45^\circ$  and the tip has an influence towards the preferred chirality [138]. Although a qualitative interpretation of this behavior is given, quantitatively modeling of this phenomenon was not achieved until recently [169]. A FEM simulation approach is employed to model this behavior [Fig. 31(b)]. A bilayer nanoribbon of length  $L = 3.2 \mu\text{m}$ , width  $w = 0.1 \mu\text{m}$ , thickness  $h_1 = h_2 = 5 \text{ nm}$ , and misfit strain  $\varepsilon_0 = 0.05$  is partitioned into two connected regions

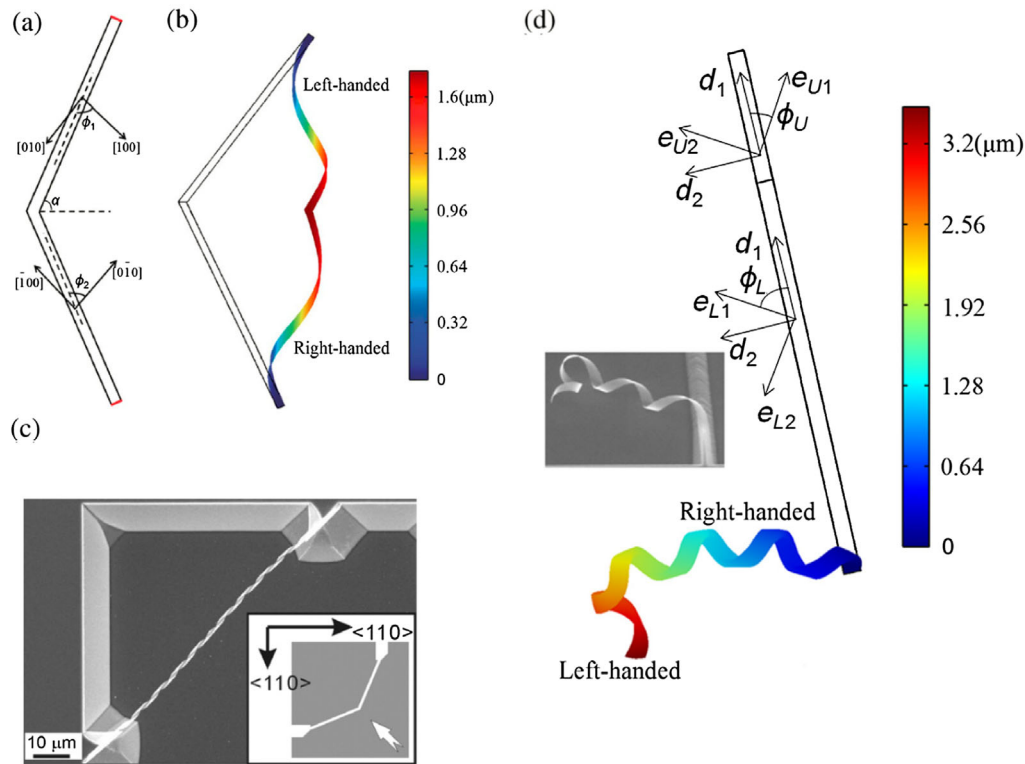


FIG. 31. (a) Geometry of a symmetric mesa design. Both ends (in red) are fixed. (b) A strained nanoribbon with symmetric left-handed and right-handed segments (both ends being fixed). Here,  $\theta_1 = \theta_2 = 75^\circ$ , and  $\varepsilon_0 = 0.024$ . (c) SEM image of a typical helical structure (diameter of  $1.4 \mu\text{m}$ ) formed by a V-shaped mesa with both ends fixed to the substrate. The two arms of the V-shaped mesa form helices, with opposite chirality. The inset shows the mesa design and the rolling direction of the helix as indicated with a white arrow. (d) A helical nanoribbon with both left-handed and right-handed segments with only one fixed end. Here,  $\theta_L = 50^\circ$ ,  $\theta_U = 40^\circ$ , and  $\varepsilon_0 = 0.05$ . In the upper segment (of length  $0.8 \mu\text{m}$ ), the effective misfit strain tensor of the bottom layer is  $\varepsilon_b = \varepsilon_0 e_{U2} \otimes e_{U2}$ . In the lower segment (of length  $2.4 \mu\text{m}$ ), the effective misfit strain tensor of the bottom layer is  $\varepsilon_b = \varepsilon_0 e_{L2} \otimes e_{L2}$ . The color indicates the total displacement. (a), (b), and (d) are adapted from Ref. [169] with permission of The Royal Society of Chemistry. (c) and the inset of (d) are adapted from Ref. [138] (© IOP Publishing, reproduced with permission, all rights reserved).

of length 0.8 and  $2.4 \mu\text{m}$ , respectively. The misalignment angle between the ribbon's long axis and the major bending axis  $\langle 100 \rangle$  in the lower part and the upper part are both  $50^\circ$ . The resulting simulation shows the coexistence of both left- and right-handed segments separated by a short perversion [11,177], in agreement with the experimental observations made by Zhang *et al.* [138] [Fig. 31(d)]. Nevertheless, the physical mechanism of this perversion is different from that of tendrill perversions, since the boundary conditions are different.

## VI. MULTISTABILITY IN STRAINED MULTILAYER SYSTEMS

Some mechanical structures can exhibit more than one stable shape [10,42,62,63,71,88]. For example, the lobes of the Venus flytrap (*Dionaea*) can be triggered to snap within a fraction of a second to capture insects [180]. Slap bracelets and tape springs are another set of multistable structures [13]. In recent years, multistable structures have received much attention because of their applications in micropumps, valves, deployable aerospace structures [10],

mechanical memory cells [71], artificial muscles, bioinspired robots [19], and energy-harvesting devices [43]. Such structures inspire the design of deployable or smart actuation devices with multiple stable shapes, each of which can function independently.

### A. Multistability in Venus flytrap and bioinspired structures

Forterre *et al.* [180] use the mechanical instability principle to interpret the snap-through of the leaves in the Venus flytrap. They put arrays of UV fluorescent markers on the surface of the leaves to calculate the principal curvatures ( $\kappa_x$  and  $\kappa_y$ ). In their experiment, an ultraviolet light is used to irradiate the Venus flytrap and a high-speed camera videotapes the trap-closure process. From the recorded data, the researchers adopt the spatially averaged Gaussian curvature and mean curvature in order to simplify the analysis. Leaf-cutting experiments are also performed to measure the intrinsic principal curvatures in a closed trap, as shown in Fig. 32(a). Moreover, a simple model based on elasticity theory is proposed which takes

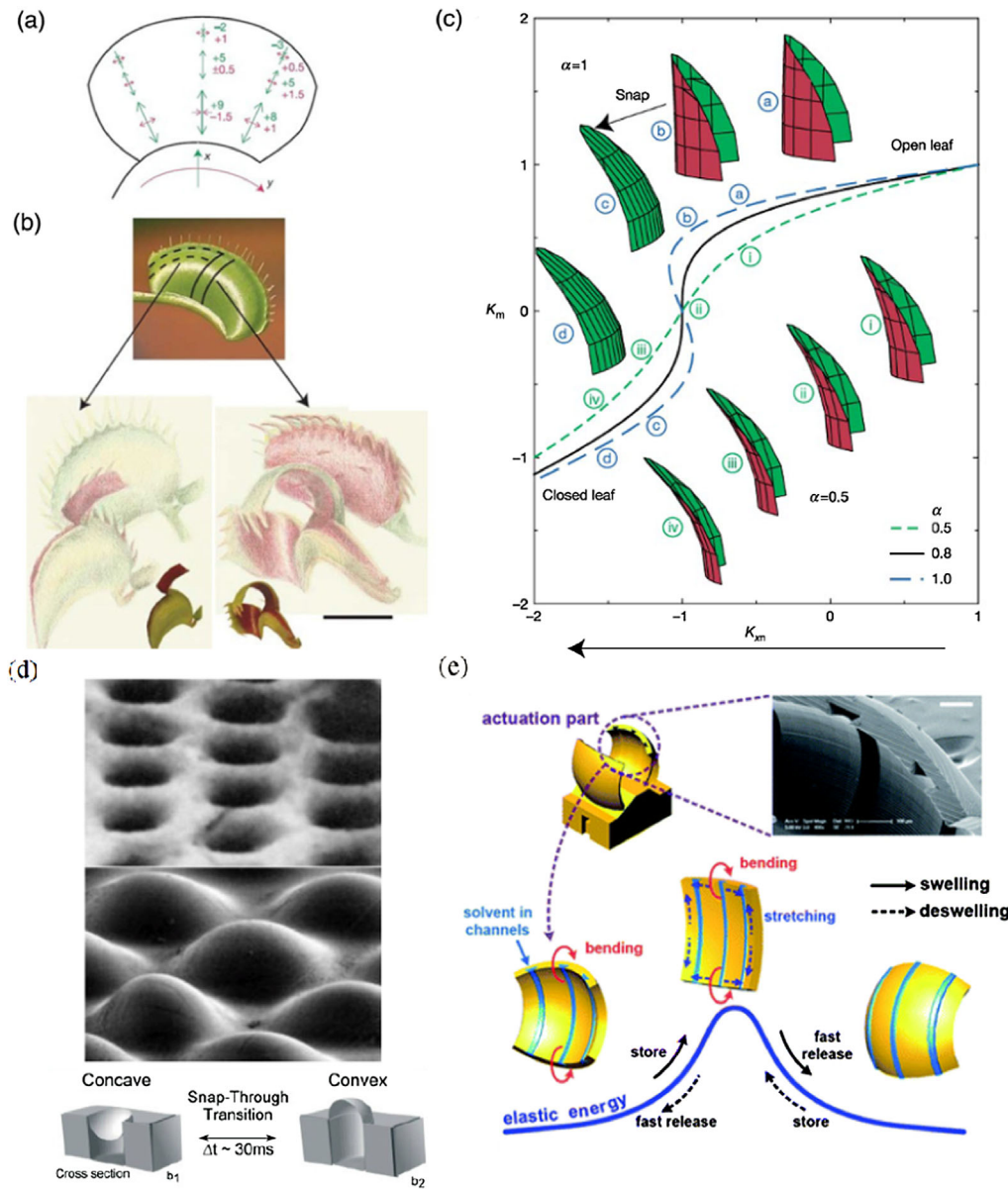


FIG. 32. (a) Measurement of the strain field; (b) the closed leaf is cut to illustrate the natural principal curvatures; (c) mean curvature as  $K_m$  a function of  $K_{xm}$ . (a)–(c) are reprinted with permission from Macmillan Publishers Ltd: Nature, Ref. [180] (© 2005). (d) Snapping surface of concave microlenses that mimics the Venus flytrap. Adapted from Ref. [181] with permission (© 2007). (e) A swelling-induced snapping microbot made of hydrogel shell with microfluidic channels embedded (a scanning electron microscope image embedded). Adapted from Ref. [182] with permission from The Royal Society of Chemistry.

into account the nontrivial coupling between the bending and stretching of a plate. The leaf is modeled as a thin elastic shell with a radius  $L$ , thickness  $H$ , Young's modulus  $E$ , and intrinsic principal curvatures  $\kappa_{x0}$  and  $\kappa_{y0}$ . It is assumed that, at time  $t = 0$ ,  $\kappa_x = \kappa_y = \kappa_{y0} = \kappa$  in order to simplify the analysis. The total elastic energy at time  $t$  is  $U = U_{\text{bending}} + U_{\text{stretching}} = (K_x - K_{x0})^2 + (K_y - 1)^2 + \alpha(K_x K_y - 1)^2$ , where  $K_i = \kappa_i/\kappa$  ( $i = x, y$ ) are the normalized principal curvatures and  $\kappa$  is the denormalization factor for the principal curvatures. The dimensionless parameter  $\alpha \sim L^4 \kappa^2 / H^2$  depicts the nonlinear coupling between bending and stretching.

By minimizing the total energy with respect to  $K_x$  and  $K_y$  (i.e.,  $(\partial U / \partial K_1) = (\partial U / \partial K_2) = 0$ ), at different values of  $\alpha$ , the leaf shape can be resolved as a function of  $K_{x0}$ . It is then shown that the dimensionless parameter  $\alpha$ , which is related to the size, thickness, and curvature, controls the

bistability of the Venus flytrap [Fig. 32(b)]. In particular, when  $\alpha < \alpha_c \approx 0.8$ , the system has only one minimum energy state; when  $\alpha > \alpha_c \approx 0.8$ , the system becomes multistable [Fig. 32(b)].

Inspired by the Venus flytrap, Holmes and Crosby use a mechanical buckling mechanism to create bistable snapping surfaces [181]. Figure 32(d) shows doubly curved bistable shells generated through biaxial compression. PDMS patterned with holes is prestretched and cross-linked with a top layer of uncured PDMS. This forms concave and convex microlenses that exhibit snap-through. Varying geometric parameters such as lens size and spacing can control the curvature of these lenses.

Lee, Xia, and Fang [182] further design snapping robots using a similarly bioinspired strategy. A jumping microgel device is manufactured as shown in Fig. 32(e). By creating a dome-shaped hydrogel shell that can swell or deswell in

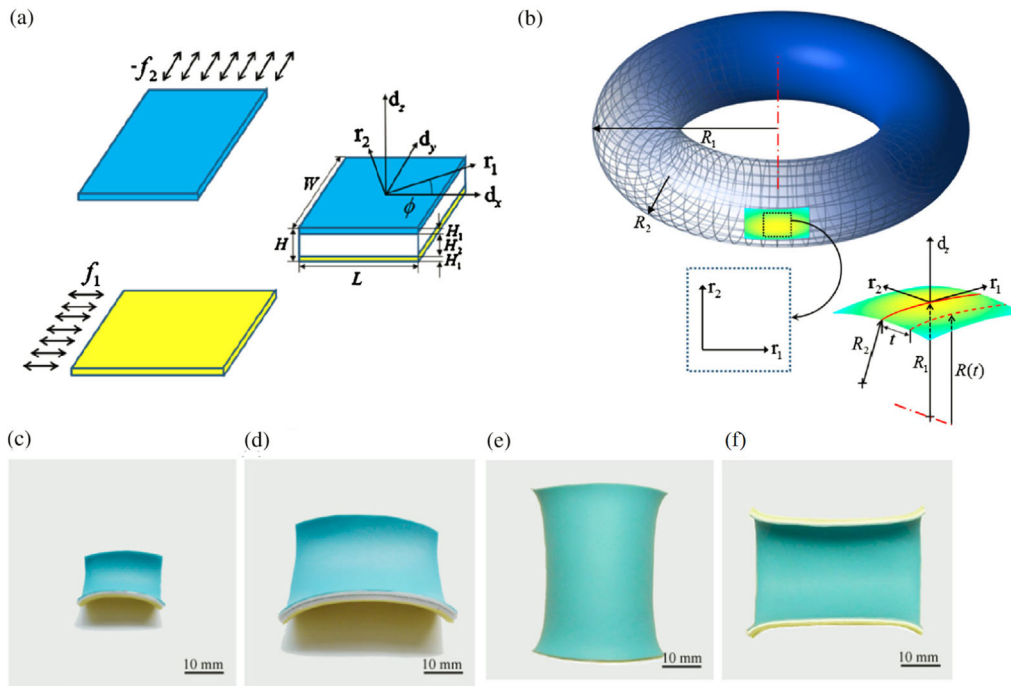


FIG. 33. (a) Blue and yellow latex sheets are perpendicularly prestretched and bonded to a thicker elastic strip. The multilayer sheet forms a doubly curved shape that conforms to a torus (b). Small (c) and large (d) thin squares form saddles, while thin strips (e), (f) form stable semicylinders. Reprinted with permission from Ref. [185] (© 2012 by the American Physical Society).

response to external stimuli and employing elastic instability, the researchers are able to achieve rapid actuation. The self-jumping device can accomplish a snap-through motion within a period of 12 ms. Upon swelling, the microgel legs of the device snap-buckle, resulting in a rapid jump. The power density of this device approaches that of a human muscle.

Shankar *et al.* [183] show that a lightweight snap-through actuator can be designed through the use of azobenzene-functionalized polymers. By using bistable arches, the authors are able to generate a snap-through with a speed as high as 100 mm/s. These actuators buckle in response to light, making them especially suitable as small remotely and precisely triggerable actuators. Leong *et al.* [184] produce a similar snapping microgripper structure that can be remotely activated by both chemicals and heat. These grippers can be used to perform cellular-scale tasks on command.

### B. Bistable and neutral stable shells

Chen *et al.* [185] develop a theoretical model to study bistability in strained multilayer systems complemented with tabletop experiments. Monostable and bistable shapes are manufactured by prestretching two pieces of rubber sheets uniaxially along perpendicular directions and then bonded with a layer of adhesive elastic sheet made of acrylic [Figs. 33(a) and 33(c)–33(f)]. The composite layers can be either monostable or bistable depending on the geometric dimensions: They are monostable when the system is either narrow or thick but bistable otherwise. The geometric and mechanical conditions of bistability are studied through a theoretical model that models the

deformation of an initially flat elastic strip onto the surface of a torus [Fig. 33(b)] with two geometric parameters ( $\kappa_1$  and  $\kappa_2$ ). By comparing the bending and in-plane stretching energy in the model, two dimensionless parameters (the first related to both the mechanical driving forces and geometric parameters, and the second purely associated with the forces) are identified to be controlling bistability. The first parameter,  $\xi = \sqrt{f/EHW}/H$ , involves the surface stress  $f$ , the Young's modulus  $E$ , the width  $W$ , and the thickness  $H$ . When it is below the threshold value, the multilayer system is monostable, as shown in Figs. 34(c) and 34(d); when it goes beyond the threshold, the system becomes bistable [Figs. 34(e) and 34(f)]. Noticeably, the parameter  $\xi$  is essentially equivalent to the geometric parameter  $\eta \equiv W\sqrt{\kappa}/H$  [15,149,185], but the former does not involve the unknown curvature  $\kappa$  and, therefore, is more suitable for the purpose of designing multistable structures. Guo *et al.* [22] employ this model to address the shape transition and associated change in multistability as discussed before.

The second parameter,  $\beta \equiv f_2/f_1$ , dictates the nature of the multistability.  $\beta < 0$  is a necessary but not a sufficient condition for bistability [Figs. 34(a) and 34(e)–34(g)]; when  $\beta \equiv 1$ , the system can exhibit neutral stability [Figs. 34(c) and 34(h)] if the first parameter  $\xi$  is above the critical value.

In fact, structures featuring neutral stability have been created as zero-stiffness elastic structures [16,186,187]. Guest and co-workers study a prestressed shell structure that can deform with zero twist rigidity as shown in Fig. 34(h). Experiments and analytical modeling have been carried out to gain insights on such mechanical properties [186,187]. Guest *et al.* [186] propose a simple analytical

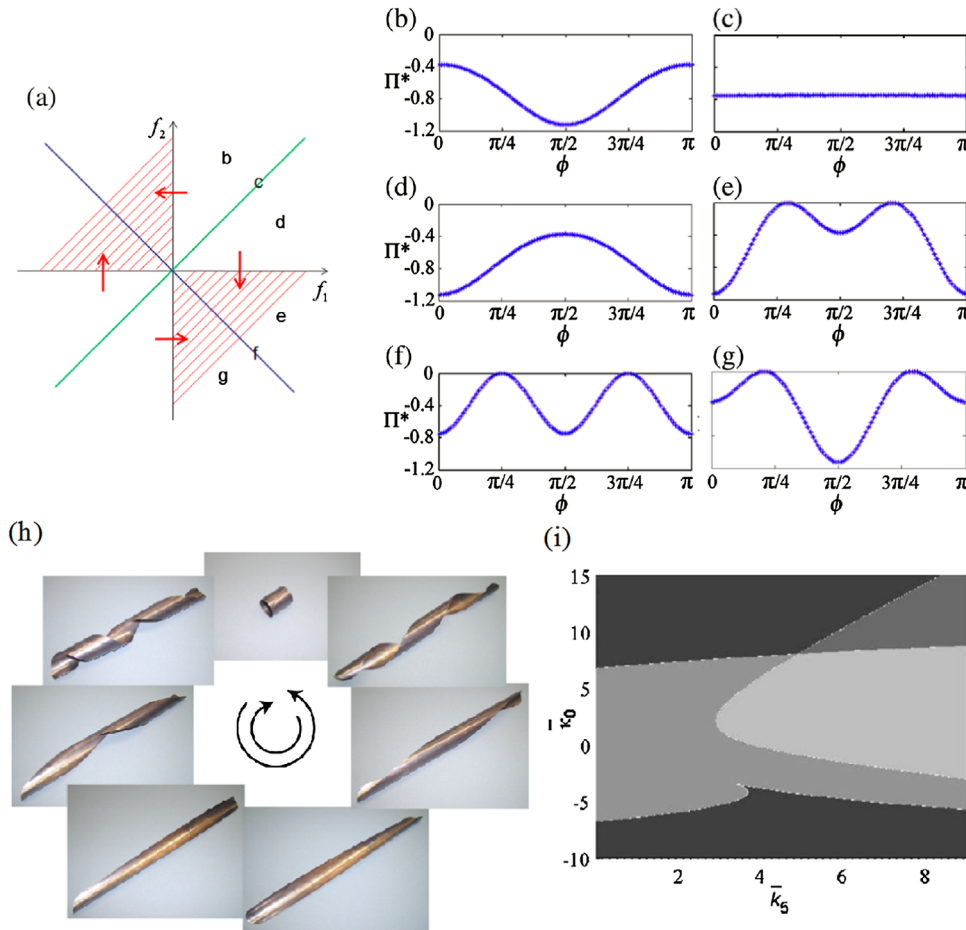


FIG. 34. (a) Multistable shell design space, with bistability in red. (b)–(g) Total strain energy as a function of misfit axis orientation, for orientations  $f_2/f_1 = \sqrt{3}$ ,  $f_2/f_1 = 1$ ,  $f_2/f_1 = 1/\sqrt{3}$ ,  $f_2/f_1 = -1/\sqrt{3}$ ,  $f_2/f_1 = -1$ , and  $f_2/f_1 = -\sqrt{3}$ . (a)–(g) are reprinted with permission from Ref. [185] (© 2012 by the American Physical Society). (h) A variety of shapes of a prestressed shell structure with zero stiffness. The shell can be transformed from one configuration to another along either the clockwise or anticlockwise path, and each shape can be held merely by friction with the table's surface. First published in Journal of Mechanics of Materials and Structure in 2011, from Ref. [186] (published by Mathematical Sciences Publishers © 2011). (i) is adapted from Ref. [187] with permission (© 2011 ASME).

model based on the assumption that the shell is not extensional and that the curvature is uniform throughout the shell (neglecting possible edge effects). As a result, the shell's midplane can be considered to lie on the surface of a cylinder, and bending along any arbitrary axis is energetically equally favorable. Seffen and Guest [187] modify these governing equations to obtain analytical solutions for both the opposite-sense and same-sense prestressed shells

that exhibit bistability and neutral stability, respectively. For isotropic materials, previous studies show that an elastic shell enters a neutrally stable state (with zero twist rigidity) under same-sense prestressing when the prestress is sufficiently large, which is observed in heated plates [188] although it had not been quantitatively characterized as in a neutral stable state until recently [186,187]. By contrast, opposite-sense prestressing can result in a bistable

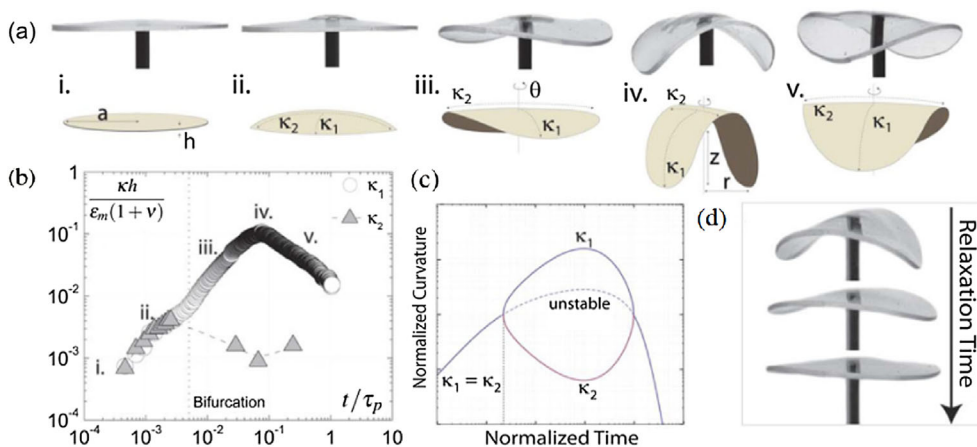


FIG. 35. (a) Images and schematic diagrams of a circular disk buckles axisymmetrically with principal curvatures  $\kappa_1 = \kappa_2$  and bifurcates with two distinct positive curvatures. (b) Normalized curvature versus nonhomogeneously swollen time. (c) By minimizing the total strain energy, the relationship between normalized curvature and normalized time is obtained and is in good agreement with experimental data. (d) The circular disk relaxes back to its original flat state. Adapted from Ref. [16] with permission of The Royal Society of Chemistry.

state when the driving force is large enough, which is similar to a bifurcation phenomenon first studied by Hyer that occurred during the curing of unsymmetrical laminates. Hyer discovered that a flat plate with anisotropic mechanical properties deforms initially into a saddle shape with a negative Gauss curvature, but when the curing temperature further increases, the shell can no longer be stable in a doubly curved shape and bifurcates into a configuration with nearly zero Gauss curvature, albeit with two opposite bending directions [188].

The mechanisms for such bifurcation phenomena have since been investigated by a number of researchers [15,16,185,187–190]. Holmes *et al.* [16] investigate the bending of slender cross-linked polydimethylsiloxane beams by soaking one side of the beams in one of two different solvents (analogous to applying a thermal gradient) and measure the resulting curvature over time. They then develop analytic solutions that provide quantitative characterization of curvature time scales and normalized parameters. It is found that the beams bend quickly to their maximum curvature but relax slowly. The author further investigates axial symmetric quasi-2D disks characterized by two principal curvatures [Figs. 35(a)–35(d)]. When bifurcation occurs, the Karman plate theory predicts that the two principal curvatures become unequal in magnitude and rotate azimuthally, while the material points stay horizontally locked. This phenomenon, analogous to thermal swelling, is experimentally verified by marking points on the plates—during dynamic rotation, the points move only in the vertical direction.

Moreover, researchers design and study devices consisting of multiple prestressed pieces to exhibit multistability [191,192]. For example, Lachenal, Weaver, and Daynes [191] create a joined structure from two prestressed flanges to have two stable shapes and analyze the mechanical behaviors by using a combination of experiments, finite-element analysis, and a simple analytical model. Pirrera *et al.* [192] further develop cylindrical lattices comprised of hinged helical strips to exhibit bistability and neutral stability that mimic the multistable behaviors of the virus bacteriophage T4. These multistable structures can serve as outstanding candidates for energy-absorption devices, morphing structures, and deployable structures for a variety of engineering applications.

## VII. OUTLOOK

This review provides a comprehensive overview of state-of-the-art techniques for mechanical self-assembly of strain-engineered flexible layers. By programming prescribed strain into these flexible layers, they can be made to wrinkle, roll, or twist predictably both at manufacturing and when activated by stimuli. We explore the mechanics of strain-induced bending multilayers as well as of spontaneous helix formation and show experimental examples manufactured from materials such as hydrogel bilayers and

liquid-crystal polymer networks. Shape transitions and multistability in the resulting structures, including in helical ribbons, are also discussed. In order to limit the article's length, certain aspects of large soft layer deformation like creasing instability [187,188] are not discussed. Various methods to harness this kind of nonlinear behavior are shown in a recent review [193].

While there have been significant advances in techniques to manufacture self-assembling strain-engineered layers, gaps remain in our understanding of folding mechanics, and large improvements in the mechanical properties of most layers are necessary before they are commercially viable. Shape-morphing layers are also slower and weaker than other classes of actuators. Although piezoelectric materials can actuate on the order of milliseconds, composites that rely on changes in temperature, humidity, or light take minutes or hours to fully morph from one shape to another. Certain voltage-stimulated polymer composites can lift many times their own weight, but most layers can lift only a small fraction. This is a result of both the relative slowness of environmental signals and their very-low-energy density. In addition, some layers have significant issues with hysteresis, which limits their ability to be reused [194–196]. More work needs to be done both in improving environment-triggered layers for use in adaptive surfaces and in developing flexible materials that can actuate in response to more energy-dense chemical or electrical triggers.

Shape-morphing flexible layers have a wide range of applications as sensors, actuators, and adaptive surfaces. Because they passively actuate in response to environmental changes like temperature, humidity, salinity, and pH, these materials and structures make excellent candidates for environment sensors. Unlike traditional passive sensors, flexible layers can adopt any shape, and thus it is significantly easier to add them to structures and devices. In addition, their thin profile and potential sensitivity make them suitable for artificial skin, as they are simpler than the matrices of hard sensors currently used in the field. Their small footprint and low material cost allow them to be constructed cheaply and efficiently.

One can also imagine broad uses as passive actuators, such as blinds that open and close in response to temperature and sunlight or solar-panel actuators that mimic plants to track the movement of the Sun. Passive solar-panel movement increases the overall efficiency of the panels, which can add up to a huge amount of energy over large installations. Briefly discussed in the review are layers that exhibit multistability over a single stimulus. This behavior, if harnessed through clever engineering as actuation for an origami robot, could allow the robot to function indefinitely without an onboard power source. This is important primarily for scientific robots operating in extreme environments such as the deep sea, arctic tundra, and other planets. If the robot can passively or semipassively move

autonomously, it frees up power for scientific instruments. More broadly, self-assembling layers that transition under stimuli are useful for all systems where functionality is to be built into the form.

### ACKNOWLEDGMENTS

This work is supported by the Society in Science-Branco Weiss fellowship administered by ETH Zürich (Z. C.), the Natural Science Foundation of China (No. 51322201 and No. 51475093), and Science and Technology Commission of Shanghai Municipality (No. 12520706300).

Z. C., G. H., and I. T. contributed equally to this work.

- 
- [1] Y. Sawa, K. Urayama, T. Takigawa, V. Gimenez-Pinto, B. L. Mbang, F. F. Ye, J. V. Selinger, and R. L. B. Selinger, Shape and chirality transitions in off-axis twist nematic elastomer ribbons, *Phys. Rev. E* **88**, 022502 (2013).
- [2] W. M. Li, G. S. Huang, H. Yan, J. Wang, Y. Yu, X. H. Hu, X. J. Wu, and Y. F. Mei, Fabrication and stimuli-responsive behavior of flexible micro-scrolls, *Soft Matter* **8**, 7103 (2012).
- [3] J. J. Abbott, K. E. Peyer, M. C. Lagomarsino, L. Zhang, L. X. Dong, I. K. Kaliakatsos, and B. J. Nelson, How should microrobots swim?, *Int. J. Robot Res.* **28**, 1434 (2009).
- [4] T. Huang, Z. Q. Liu, G. S. Huang, R. Liu, and Y. F. Mei, Grating-structured metallic microsprints, *Nanoscale* **6**, 9428 (2014).
- [5] Q. Ge, H. J. Qi, and M. L. Dunn, Active materials by four-dimension printing, *Appl. Phys. Lett.* **103**, 131901 (2013).
- [6] G. Hwang, C. Dockendorf, D. Bell, L. Dong, H. Hashimoto, D. Poulidakos, and B. Nelson, 3-D InGaAs/GaAs Helical nanobelts for optoelectronic devices, *Int. J. Optomechatron.* **2**, 88 (2008).
- [7] J. A. Rogers, T. Someya, and Y. G. Huang, Materials and mechanics for stretchable electronics, *Science* **327**, 1603 (2010).
- [8] I. W. Hamley, A. Dehsorkhi, V. Castelletto, S. Furzeland, D. Atkins, J. Seitsonen, and J. Ruokolainen, Reversible helical unwinding transition of a self-assembling peptide amphiphile, *Soft Matter* **9**, 9290 (2013).
- [9] Z. Chen, C. Majidi, D. J. Srolovitz, and M. Haataja, Tunable helical ribbons, *Appl. Phys. Lett.* **98**, 011906 (2011).
- [10] L. Zhang, E. Ruh, D. Grutzmacher, L. X. Dong, D. J. Bell, B. J. Nelson, and C. Schonenberger, Anomalous coiling of SiGe/Si and SiGe/Si/Cr helical nanobelts, *Nano Lett.* **6**, 1311 (2006).
- [11] S. J. Gerbode, J. R. Puzey, A. G. McCormick, and L. Mahadevan, How the cucumber tendril coils and overwinds, *Science* **337**, 1087 (2012).
- [12] J. S. Huang, J. Liu, B. Kroll, K. Bertoldi, and D. R. Clarke, Spontaneous and deterministic three-dimensional curling of pre-strained elastomeric bi-strips, *Soft Matter* **8**, 6291 (2012).
- [13] E. Kebabzade, S. D. Guest, and S. Pellegrino, Bistable prestressed shell structures, *Int. J. Solids Struct.* **41**, 2801 (2004).
- [14] M. W. Hyer, The room-temperature shapes of four-layer unsymmetric, *J. Compos. Mater.* **16**, 318 (1982).
- [15] S. Armon, E. Efrati, R. Kupferman, and E. Sharon, Geometry and mechanics in the opening of chiral seed pods, *Science* **333**, 1726 (2011).
- [16] D. P. Holmes, M. Roche, T. Sinha, and H. A. Stone, Bending and twisting of soft materials by non-homogenous swelling, *Soft Matter* **7**, 5188 (2011).
- [17] T. Savin, N. A. Kurpios, A. E. Shyer, P. Florescu, H. Y. Liang, L. Mahadevan, and C. J. Tabin, On the growth and form of the gut, *Nature (London)* **476**, 57 (2011).
- [18] A. E. Shyer, T. Tallinen, N. L. Nerurkar, Z. Y. Wei, E. S. Gil, D. L. Kaplan, C. J. Tabin, and L. Mahadevan, Villification: How the gut gets its villi, *Science* **342**, 212 (2013).
- [19] N. Chouaieb, A. Goriely, and J. H. Maddocks, Helices, *Proc. Natl. Acad. Sci. U.S.A.* **103**, 9398 (2006).
- [20] J. S. Wang, X. Q. Feng, G. F. Wang, and S. W. Yu, Twisting of nanowires induced by anisotropic surface stresses, *Appl. Phys. Lett.* **92**, 191901 (2008).
- [21] Z. Chen, C. Majidi, D. J. Srolovitz, and M. Haataja, Continuum elasticity theory approach for spontaneous bending and twisting of ribbons induced by mechanical anisotropy, arXiv:1209.3321.
- [22] Q. Guo, A. K. Mehta, M. A. Grover, W. Chen, D. G. Lynn, and Z. Chen, Shape selection and multi-stability in helical ribbons, *Appl. Phys. Lett.* **104**, 211901 (2014).
- [23] S. Armon, H. Aharoni, M. Moshe, and E. Sharon, Shape selection in chiral ribbons: From seed pods to supramolecular assemblies, *Soft Matter* **10**, 2733 (2014).
- [24] Y. Sawa, F. F. Ye, K. Urayama, T. Takigawa, V. Gimenez-Pinto, R. L. B. Selinger, and J. V. Selinger, Shape selection of twist-nematic-elastomer ribbons, *Proc. Natl. Acad. Sci. U.S.A.* **108**, 6364 (2011).
- [25] W. S. Childers, N. R. Anthony, A. K. Mehta, K. M. Berland, and D. G. Lynn, Phase networks of cross-beta peptide assemblies, *Langmuir* **28**, 6386 (2012).
- [26] L. Dai and W. Z. Shen, Cosserat curve model for super-elasticity of helices, *Nanotechnology* **20**, 465707 (2009).
- [27] A. G. Shtukenberg, Y. O. Punin, A. Gujral, and B. Kahr, Growth actuated bending and twisting of single crystals, *Angew. Chem., Int. Ed.* **53**, 672 (2014).
- [28] B. Li, Y. P. Cao, X. Q. Feng, and H. J. Gao, Mechanics of morphological instabilities and surface wrinkling in soft materials: A review, *Soft Matter* **8**, 5728 (2012).
- [29] M. H. Huang, F. Cavallo, F. Liu, and M. G. Lagally, Nanomechanical architecture of semiconductor nanomembranes, *Nanoscale* **3**, 96 (2011).
- [30] Y. Wang, J. Xu, Y. W. Wang, and H. Y. Chen, Emerging chirality in nanoscience, *Chem. Soc. Rev.* **42**, 2930 (2013).
- [31] D.-B. Zhang, E. Akatyeva, and T. Dumitrică, Bending Ultrathin Graphene at the Margins of Continuum Mechanics, *Phys. Rev. Lett.* **106**, 255503 (2011).
- [32] L. Tapasztó, T. Dumitrică, S. J. Kim, P. Nemes-Incze, C. Hwang, and L. P. Biró, Breakdown of continuum mechanics for nanometre-wavelength rippling of graphene, *Nat. Phys.* **8**, 739 (2012).

- [33] K. Zhang and M. Arroyo, Adhesion and friction control localized folding in supported graphene, *J. Appl. Phys.* **113**, 193501 (2013).
- [34] B. D. Leahy, L. Pocivavsek, M. Meron, K. L. Lam, D. Salas, P. J. Viccaro, K. Y. C. Lee, and B. Lin, Geometric Stability and Elastic Response of a Supported Nanoparticle Film, *Phys. Rev. Lett.* **105**, 058301 (2010).
- [35] P. Kanjanaboos, A. Joshi-Imre, X.-M. Lin, and H. M. Jaeger, Strain patterning and direct measurement of Poisson's ratio in nanoparticle monolayer sheets, *Nano Lett.* **11**, 2567 (2011).
- [36] Y. Chua, B. Leahy, M. Zhang, S. You, K. Y. C. Lee, S. N. Coppersmith, and B. Lin, Incommensurate phases of a supported nanoparticle film subjected to uniaxial compression, *Proc. Natl. Acad. Sci. U.S.A.* **110**, 824 (2013).
- [37] Y. Wang, P. Kanjanaboos, S. P. McBride, E. Barry, X.-M. Lin, and H. M. Jaeger, Mechanical properties of self-assembled nanoparticle membranes: stretching and bending, *Faraday Discuss.* **181**, 325 (2015).
- [38] E. Hobbie, D. Simien, J. Fagan, J. Huh, J. Chung, S. Hudson, J. Obrzut, J. Douglas, and C. Stafford, Wrinkling and Strain Softening in Single-Wall Carbon Nanotube Membranes, *Phys. Rev. Lett.* **104**, 125505 (2010).
- [39] J. M. Harris, J. Y. Huh, M. R. Semler, T. Ihle, C. M. Stafford, S. D. Hudson, J. A. Fagan, and E. K. Hobbie, Elasticity and rigidity percolation in flexible carbon nanotube films on PDMS substrates, *Soft Matter* **9**, 11568 (2013).
- [40] M. R. Semler, J. M. Harris, and E. K. Hobbie, Wrinkling and folding of nanotube-polymer bilayers, *J. Chem. Phys.* **141**, 044901 (2014).
- [41] J. Rodríguez-Hernández, Wrinkled interfaces: Taking advantage of surface instabilities to pattern polymer surfaces, *Prog. Polym. Sci.* **42**, 1 (2015).
- [42] A. I. Fedorchenko, A.-B. Wang, V. I. Mashanov, W.-P. Huang, and H. H. Cheng, Strain-induced wrinkling on SiGe free standing film, *Appl. Phys. Lett.* **89**, 043119 (2006).
- [43] G. Huang and Y. Mei, Thinning and shaping solid films into functional and integrative nanomembranes, *Adv. Mater.* **24**, 2517 (2012).
- [44] O. G. Schmidt and K. Eberl, Nanotechnology: Thin solid films roll up into nanotubes, *Nature (London)* **410**, 168 (2001).
- [45] F. Brau, H. Vandeparre, A. Sabbah, C. Poulard, A. Boudaoud, and P. Damman, Multiple-length-scale elastic instability mimics parametric resonance of nonlinear oscillators, *Nat. Phys.* **7**, 56 (2011).
- [46] Y. Ebata, A. B. Croll, and A. J. Crosby, Wrinkling and strain localizations in polymer thin films, *Soft Matter* **8**, 9086 (2012).
- [47] Y. Mei, S. Kiravittaya, S. Harazim, and O. G. Schmidt, Principles and applications of micro and nanoscale wrinkles, *Mater. Sci. Eng. R* **70**, 209 (2010).
- [48] J.-Y. Sun, S. Xia, M.-W. Moon, K. H. Oh, and K.-S. Kim, Folding wrinkles of a thin stiff layer on a soft substrate, *Proc. R. Soc. A* **468**, 932 (2012).
- [49] M. R. Semler, J. M. Harris, A. B. Croll, and E. K. Hobbie, Localization and length-scale doubling in disordered films on soft substrates, *Phys. Rev. E* **88**, 032409 (2013).
- [50] O. Oshri, F. Brau, and H. Diamant, Wrinkles and folds in a fluid-supported sheet of finite size, *Phys. Rev. E* **91**, 052408 (2015).
- [51] J. Zang, X. Zhao, Y. Cao, and J. W. Hutchinson, Localized ridge wrinkling of stiff films on compliant substrates, *J. Mech. Phys. Solids* **60**, 1265 (2012).
- [52] P. Cendula, S. Kiravittaya, Y. Mei, C. Deneke, and O. Schmidt, Bending and wrinkling as competing relaxation pathways for strained free-hanging films, *Phys. Rev. B* **79**, 085429 (2009).
- [53] Z. Budrikis, A. L. Sellerio, Z. Bertalan, and S. Zapperi, Wrinkle motifs in thin films, *Sci. Rep.* **5**, 8938 (2015).
- [54] W. M. Choi, J. Song, D.-Y. Khang, H. Jiang, Y. Y. Huang, and J. A. Rogers, Biaxially stretchable "wavy" silicon nanomembranes, *Nano Lett.* **7**, 1655 (2007).
- [55] C. Deneke, C. Müller, N. Jin-Phillipp, and O. Schmidt, Diameter scalability of rolled-up In (Ga) As/GaAs nanotubes, *Semicond. Sci. Technol.* **17**, 1278 (2002).
- [56] P. Froeter, X. Yu, W. Huang, F. Du, M. Li, I. Chun, S. H. Kim, K. J. Hsia, J. A. Rogers, and X. Li, 3D hierarchical architectures based on self-rolled-up silicon nitride membranes, *Nanotechnology* **24**, 475301 (2013).
- [57] W. Huang, S. Koric, X. Yu, K. J. Hsia, and X. Li, Precision structural engineering of self-rolled-up 3D nanomembranes guided by transient quasi-static FEM modeling, *Nano Lett.* **14**, 6293 (2014).
- [58] X. Li, Strain induced semiconductor nanotubes: From formation process to device applications, *J. Phys. D* **41**, 193001 (2008).
- [59] J. Xiao, A. Carlson, Z. Liu, Y. Huang, H. Jiang, and J. Rogers, Stretchable and compressible thin films of stiff materials on compliant wavy substrates, *Appl. Phys. Lett.* **93**, 013109 (2008).
- [60] Y. Zhang *et al.*, Experimental and theoretical studies of serpentine microstructures bonded to prestrained elastomers for stretchable electronics, *Adv. Funct. Mater.* **24**, 2028 (2014).
- [61] L. D. Landau and E. M. Lifshitz, *Theory of Elasticity*, 3rd ed. (Pergamon, New York, 1986).
- [62] T. Mora and A. Boudaoud, Buckling of swelling gels, *Eur. Phys. J. E* **20**, 119 (2006).
- [63] I. S. Chun, A. Challa, B. Derickson, K. J. Hsia, and X. Li, Geometry effect on the strain-induced self-rolling of semiconductor membranes, *Nano Lett.* **10**, 3927 (2010).
- [64] P. Cendula, A. Malachias, C. Deneke, S. Kiravittaya, and O. G. Schmidt, Experimental realization of coexisting states of rolled-up and wrinkled nanomembranes by strain and etching control, *Nanoscale* **6**, 14326 (2014).
- [65] P. Cendula, S. Kiravittaya, I. Mönch, J. Schumann, and O. G. Schmidt, Directional roll-up of nanomembranes mediated by wrinkling, *Nano Lett.* **11**, 236 (2011).
- [66] H. King, R. D. Schroll, B. Davidovitch, and N. Menon, Elastic sheet on a liquid drop reveals wrinkling and crumpling as distinct symmetry-breaking instabilities, *Proc. Natl. Acad. Sci. U.S.A.* **109**, 9716 (2012).
- [67] G. M. Grason and B. Davidovitch, Universal collapse of stress and wrinkle-to-scar transition in spherically confined crystalline sheets, *Proc. Natl. Acad. Sci. U.S.A.* **110**, 12893 (2013).

- [68] Y. Mei, D. J. Thurmer, F. Cavallo, S. Kiravittaya, and O. G. Schmidt, Semiconductor sub-micro-/nanochannel networks by deterministic layer wrinkling, *Adv. Mater.* **19**, 2124 (2007).
- [69] A. Malachias, Y. Mei, R. K. Annabattula, C. Deneke, P. R. Onck, and O. G. Schmidt, Wrinkled-up nanochannel networks: Long-range ordering, scalability, and X-ray investigation, *ACS Nano* **2**, 1715 (2008).
- [70] Y. Sun, W. M. Choi, H. Jiang, Y. Y. Huang, and J. A. Rogers, Controlled buckling of semiconductor nanoribbons for stretchable electronics, *Nat. Nanotechnol.* **1**, 201 (2006).
- [71] Q. Guo, M. Zhang, Z. Xue, L. Ye, G. Wang, G. Huang, Y. Mei, X. Wang, and Z. Di, Three dimensional strain distribution of wrinkled silicon nanomembranes fabricated by rolling-transfer technique, *Appl. Phys. Lett.* **103**, 264102 (2013).
- [72] W. R. Childs, M. J. Motala, K. J. Lee, and R. G. Nuzzo, Masterless soft lithography: Patterning UV/ozone-induced adhesion on poly (dimethylsiloxane) surfaces, *Langmuir* **21**, 10096 (2005).
- [73] D. C. Duffy, J. C. McDonald, O. J. Schueller, and G. M. Whitesides, Rapid prototyping of microfluidic systems in poly (dimethylsiloxane), *Anal. Chem.* **70**, 4974 (1998).
- [74] Y. Y. Huang, W. Zhou, K. Hsia, E. Menard, J.-U. Park, J. A. Rogers, and A. G. Alleyne, Stamp collapse in soft lithography, *Langmuir* **21**, 8058 (2005).
- [75] Y. Sun and J. A. Rogers, Inorganic semiconductors for flexible electronics, *Adv. Mater.* **19**, 1897 (2007).
- [76] D. H. Kim and J. A. Rogers, Stretchable electronics: Materials strategies and devices, *Adv. Mater.* **20**, 4887 (2008).
- [77] D.-Y. Khang, J. A. Rogers, and H. H. Lee, Mechanical buckling: Mechanics, metrology, and stretchable electronics, *Adv. Funct. Mater.* **19**, 1526 (2009).
- [78] J. Genzer and J. Groenewold, Soft matter with hard skin: From skin wrinkles to templating and material characterization, *Soft Matter* **2**, 310 (2006).
- [79] M. C. Cross and P. C. Hohenberg, Pattern formation outside of equilibrium, *Rev. Mod. Phys.* **65**, 851 (1993).
- [80] N. Bowden, S. Brittain, A. G. Evans, J. W. Hutchinson, and G. M. Whitesides, Spontaneous formation of ordered structures in thin films of metals supported on an elastomeric polymer, *Nature (London)* **393**, 146 (1998).
- [81] S. Chung, J. H. Lee, M. W. Moon, J. Han, and R. D. Kamm, Non-lithographic wrinkle nanochannels for protein preconcentration, *Adv. Mater.* **20**, 3011 (2008).
- [82] J. Y. Chung, T. Q. Chastek, M. J. Fasolka, H. W. Ro, and C. M. Stafford, Quantifying residual stress in nanoscale thin polymer films via surface wrinkling, *ACS Nano* **3**, 844 (2009).
- [83] Y. Karade, S. A. Pihan, W. H. Brunger, A. Dietzel, R. Berger, and K. Graf, Determination of cross-link density in ion-irradiated polystyrene surfaces from rippling, *Langmuir* **25**, 3108 (2009).
- [84] Z. Suo, E. Ma, H. Gleskova, and S. Wagner, Mechanics of rollable and foldable film-on-foil electronics, *Appl. Phys. Lett.* **74**, 1177 (1999).
- [85] A. J. Baca, J.-H. Ahn, Y. Sun, M. A. Meitl, E. Menard, H.-S. Kim, W. M. Choi, D.-H. Kim, Y. Huang, and J. A. Rogers, Semiconductor wires and ribbons for high-performance flexible electronics, *Angew. Chem., Int. Ed.* **47**, 5524 (2008).
- [86] D.-H. Kim, J.-H. Ahn, W. M. Choi, H.-S. Kim, T.-H. Kim, J. Song, Y. Y. Huang, Z. Liu, C. Lu, and J. A. Rogers, Stretchable and foldable silicon integrated circuits, *Science* **320**, 507 (2008).
- [87] Y. Mei, S. Kiravittaya, M. Benyoucef, D. J. Thurmer, T. Zander, C. Deneke, F. Cavallo, A. Rastelli, and O. G. Schmidt, Optical properties of a wrinkled nanomembrane with embedded quantum well, *Nano Lett.* **7**, 1676 (2007).
- [88] C. G. Van, de Walle, Band lineups and deformation potentials in the model-solid theory, *Phys. Rev. B* **39**, 1871 (1989).
- [89] S. P. Timoshenko and J. M. Gere, *Theory of Elastic Stability* (McGraw-Hill, New York, 1961).
- [90] Z. Huang, W. Hong, and Z. Suo, Nonlinear analyses of wrinkles in a film bonded to a compliant substrate, *J. Mech. Phys. Solids* **53**, 2101 (2005).
- [91] J. i. Takahashi and T. Makino, Raman scattering measurement of silicon-on-insulator substrates formed by high-dose oxygen-ion implantation, *J. Appl. Phys.* **63**, 87 (1988).
- [92] F. Cavallo and M. G. Lagally, Semiconductors turn soft: Inorganic nanomembranes, *Soft Matter* **6**, 439 (2010).
- [93] P. G. Evans, D. S. Timberg, M. M. Roberts, M. G. Lagally, Y. Xiao, B. Lai, and Z. Cai, Germanium hut nanostressors on freestanding thin silicon membranes, *Appl. Phys. Lett.* **87**, 073112 (2005).
- [94] Y. Mei, G. Huang, A. A. Solovev, E. Bermudez Urena, I. Monch, F. Ding, T. Reindl, R. K. Y. Fu, P. K. Chu, and O. G. Schmidt, Versatile approach for integrative and functionalized tubes by strain engineering of nanomembranes on polymers, *Adv. Mater.* **20**, 4085 (2008).
- [95] V. Y. Prinz, V. A. Seleznev, A. K. Gutakovskiy, A. V. Chehovskiy, V. V. Preobrazhenskii, M. A. Putyato, and T. A. Gavrilova, Free-standing and overgrown InGaAs/GaAs nanotubes, nanohelices and their arrays, *Physica (Amsterdam) E* **6**, 828 (2000).
- [96] A. Cho, Nanotechnology. Pretty as you please, curling films turn themselves into nanodevices, *Science* **313**, 164 (2006).
- [97] S. Golod, V. Y. Prinz, V. Mashanov, and A. Gutakovskiy, Fabrication of conducting GeSi/Si micro-and nanotubes and helical microcoils, *Semicond. Sci. Technol.* **16**, 181 (2001).
- [98] F. Liu, M. G. Lagally, and J. Zang, Nanomechanical architectures—mechanics-driven fabrication based on crystalline membranes, *MRS Bull.* **34**, 190 (2009).
- [99] F. Cavallo, R. Songmuang, C. Ulrich, and O. Schmidt, Rolling up SiGe on insulator, *Appl. Phys. Lett.* **90**, 193120 (2007).
- [100] M. Huang, C. Boone, M. Roberts, D. E. Savage, M. G. Lagally, N. Shaji, H. Qin, R. Blick, J. A. Nairn, and F. Liu, Nanomechanical architecture of strained bilayer thin films: From design principles to experimental fabrication, *Adv. Mater.* **17**, 2860 (2005).
- [101] N. Jin-Phillipp, J. Thomas, M. Kelsch, C. Deneke, R. Songmuang, and O. Schmidt, Electron microscopy study

- on structure of rolled-up semiconductor nanotubes, *Appl. Phys. Lett.* **88**, 033113 (2006).
- [102] R. Songmuang, A. Rastelli, S. Mendach, and O. G. Schmidt, SiOx/Si radial superlattices and microtube optical ring resonators, *Appl. Phys. Lett.* **90**, 091905 (2007).
- [103] P. O. Vaccaro, K. Kubota, and T. Aida, Strain-driven self-positioning of micromachined structures, *Appl. Phys. Lett.* **78**, 2852 (2001).
- [104] J. Hu, Y. Bando, J. Zhan, M. Liao, D. Golberg, X. Yuan, and T. Sekiguchi, Single-crystalline nanotubes of IIB-VI semiconductors, *Appl. Phys. Lett.* **87**, 113107 (2005).
- [105] S. Golod, V. Y. Prinz, P. Wägli, L. Zhang, O. Kirfel, E. Deckhardt, F. Glaus, C. David, and D. Grützmacher, Freestanding SiGe/Si/Cr and SiGe/Si/SixNy/Cr microtubes, *Appl. Phys. Lett.* **84**, 3391 (2004).
- [106] M. F. Doerner and W. D. Nix, Stresses and deformation processes in thin films on substrates, *Crit. Rev. Solid State Mater. Sci.* **14**, 225 (1988).
- [107] J. Zang, M. Huang, and F. Liu, Mechanism for Nanotube Formation from Self-Bending Nanofilms Driven by Atomic-Scale Surface-Stress Imbalance, *Phys. Rev. Lett.* **98**, 146102 (2007).
- [108] V. Luchnikov, O. Sydorenko, and M. Stamm, Self-rolled polymer and composite polymer/metal micro- and nanotubes with patterned inner walls, *Adv. Mater.* **17**, 1177 (2005).
- [109] K. Kumar, B. Nandan, V. Luchnikov, E. B. Gowd, and M. Stamm, Fabrication of metallic microtubes using self-rolled polymer tubes as templates, *Langmuir* **25**, 7667 (2009).
- [110] S. Zakharchenko, E. Sperling, and L. Ionov, Fully biodegradable self-rolled polymer tubes: A candidate for tissue engineering scaffolds, *Biomacromolecules* **12**, 2211 (2011).
- [111] W. Brantley, Calculated elastic constants for stress problems associated with semiconductor devices, *J. Appl. Phys.* **44**, 534 (1973).
- [112] R. t. Cottam and G. Saunders, The elastic constants of GaAs from 2 K to 320 K, *J. Phys. C* **6**, 2105 (1973).
- [113] J. Wortman and R. Evans, Young's modulus, shear modulus, and Poisson's ratio in silicon and germanium, *J. Appl. Phys.* **36**, 153 (1965).
- [114] I. S. Chun and X. Li, Controlled assembly and dispersion of strain-induced InGaAs/GaAs nanotubes, *IEEE Trans. Nanotechnol.* **7**, 493 (2008).
- [115] W. Li, G. Huang, J. Wang, Y. Yu, X. Wu, X. Cui, and Y. Mei, Superelastic metal microspheres as fluidic sensors and actuators, *Lab Chip* **12**, 2322 (2012).
- [116] C. Deneke and O. Schmidt, Structural characterization and potential x-ray waveguiding of a small rolled-up nanotube with a large number of windings, *Appl. Phys. Lett.* **89**, 123121 (2006).
- [117] Y. Tsui and T. Clyne, An analytical model for predicting residual stresses in progressively deposited coatings Part 1: Planar geometry, *Thin Solid Films* **306**, 23 (1997).
- [118] R. Songmuang, C. Deneke, and O. Schmidt, Rolled-up micro- and nanotubes from single-material thin films, *Appl. Phys. Lett.* **89**, 223109 (2006).
- [119] I. Chun, V. Verma, V. Elarde, S. Kim, J. Zuo, J. Coleman, and X. Li, InGaAs/GaAs 3D architecture formation by strain-induced self-rolling with lithographically defined rectangular stripe arrays, *J. Cryst. Growth* **310**, 2353 (2008).
- [120] L. Zhang, S. Golod, E. Deckardt, V. Prinz, and D. Grützmacher, Free-standing Si/SiGe micro- and nano-objects, *Physica (Amsterdam) E* **23**, 280 (2004).
- [121] B. Krause, C. Mocuta, T. Metzger, C. Deneke, and O. Schmidt, Local Structure of a Rolled-Up Single Crystal: An X-Ray Microdiffraction Study of Individual Semiconductor Nanotubes, *Phys. Rev. Lett.* **96**, 165502 (2006).
- [122] H. Zhen, G. Huang, S. Kiravittaya, S. Li, C. Deneke, D. J. Thurmer, Y. Mei, O. Schmidt, and W. Lu, Light-emitting properties of a strain-tuned microtube containing coupled quantum wells, *Appl. Phys. Lett.* **102**, 041109 (2013).
- [123] J. V. Selinger, M. S. Spector, and J. M. Schnur, Theory of self-assembled tubules and helical ribbons, *J. Phys. Chem. B* **105**, 7157 (2001).
- [124] K. C. Lin, R. M. Weis, and H. M. McConnell, Induction of helical liposomes by Ca<sup>2+</sup>-mediated intermembrane binding, *Nature (London)* **296**, 164 (1982).
- [125] S. Komura and O. Y. Zhong-can, High- and Low-Pitch Helical Structures of Tilted Chiral Lipid Bilayers, *Phys. Rev. Lett.* **81**, 473 (1998).
- [126] D. S. Chung, G. B. Benedek, F. M. Konikoff, and J. M. Donovan, Elastic free-energy of anisotropic helical ribbons as metastable intermediates in the crystallization of cholesterol, *Proc. Natl. Acad. Sci. U.S.A.* **90**, 11341 (1993).
- [127] R. Oda, I. Huc, M. Schmutz, S. J. Candau, and F. C. MacKintosh, Tuning bilayer twist using chiral counterions, *Nature (London)* **399**, 566 (1999).
- [128] J. M. Schnur, B. R. Ratna, J. V. Selinger, A. Singh, G. Jyothi, and K. R. K. Easwaran, Diacetylenic lipid tubules—Experimental evidence for a chiral molecular architecture, *Science* **264**, 945 (1994).
- [129] J. V. Selinger, F. C. MacKintosh, and J. M. Schnur, Theory of cylindrical tubules and helical ribbons of chiral lipid membranes, *Phys. Rev. E* **53**, 3804 (1996).
- [130] N. Nakashima, S. Asakuma, and T. Kunitake, Optical microscopic study of helical superstructures of chiral bilayer-membranes, *J. Am. Chem. Soc.* **107**, 509 (1985).
- [131] W. Helfrich and J. Prost, Intrinsic bending force in anisotropic membranes made of chiral molecules, *Phys. Rev. A* **38**, 3065 (1988).
- [132] Z. C. Ouyang and J. X. Liu, Helical Structures of Tilted Chiral Lipid Bilayers Viewed as Cholesteric Liquid-Crystals, *Phys. Rev. Lett.* **65**, 1679 (1990).
- [133] Y. V. Zastavker, N. Asherie, A. Lomakin, J. Pande, J. M. Donovan, J. M. Schnur, and G. B. Benedek, Self-assembly of helical ribbons, *Proc. Natl. Acad. Sci. U.S.A.* **96**, 7883 (1999).
- [134] J. V. Selinger and J. M. Schnur, Theory of Chiral Lipid Tubules, *Phys. Rev. Lett.* **71**, 4091 (1993).
- [135] J. S. Wang, H. M. Ye, Q. H. Qin, J. Xu, and X. Q. Feng, Anisotropic surface effects on the formation of chiral morphologies of nanomaterials, *Proc. R. Soc. A* **468**, 609 (2012).
- [136] H.-M. Ye *et al.*, Surface stress effects on the bending direction and twisting chirality of lamellar crystals of chiral polymer, *Macromolecules* **43**, 5762 (2010).

- [137] Z. Chen, X. Han, and H. Zheng, Residual stresses and Poisson's effect drive shape formation and transition of helical structures, *J. Elast.* **119**, 321 (2015).
- [138] L. Zhang, E. Deckhardt, A. Weber, C. Schonenberger, and D. Grutzmacher, Controllable fabrication of SiGe/Si and SiGe/Si/Cr helical nanobelts, *Nanotechnology* **16**, 655 (2005).
- [139] D. J. Thurmer, C. Deneke, and O. G. Schmidt, In situ monitoring of the complex rolling behaviour of InGaAs/GaAs/Nb hybrid microtubes, *J. Phys. D* **41**, 205419 (2008).
- [140] G. Wan, A. A. Solovev, G. Huang, M. F. Maitz, N. Huang, and Y. Mei, Dynamic curvature control of rolled-up metal nanomembranes activated by magnesium, *J. Mater. Chem.* **22**, 12983 (2012).
- [141] R. L. B. Selinger, J. V. Selinger, A. P. Malanoski, and J. M. Schnur, Shape Selection in Chiral Self-Assembly, *Phys. Rev. Lett.* **93**, 158103 (2004).
- [142] M. A. Wyczalkowski, Z. Chen, B. A. Filas, V. D. Varner, and L. A. Taber, Computational models for mechanics of morphogenesis, *Birth Defects Res., Part C* **96**, 132 (2012).
- [143] W. Li, G. Huang, H. Yan, J. Wang, Y. Yu, X. Hu, X. Wu, and Y. Mei, Fabrication and stimuli-responsive behavior of flexible micro-scrolls, *Soft Matter* **8**, 7103 (2012).
- [144] C. Majidi, Z. Chen, D. J. Srolovitz, and M. Haataja, Spontaneous bending of piezoelectric nanoribbons: Mechanics, polarization, and space charge coupling, *J. Mech. Phys. Solids* **58**, 73 (2010).
- [145] D. J. Bell, L. X. Dong, B. J. Nelson, M. Golling, L. Zhang, and D. Grutzmacher, Fabrication and characterization of three-dimensional InGaAs/GaAs nanosprings, *Nano Lett.* **6**, 725 (2006).
- [146] L. X. Dong, L. Zhang, B. E. Kratochvil, K. Y. Shou, and B. J. Nelson, Dual-chirality helical nanobelts: Linear-to-rotary motion converters for three-dimensional microscopy, *J. Microelectromech. Syst.* **18**, 1047 (2009).
- [147] L. Dai and L. Zhang, Directional scrolling of SiGe/Si/Cr nanoribbon on Si(111) surfaces controlled by two-fold rotational symmetry underetching, *Nanoscale* **5**, 971 (2013).
- [148] L. Dai and W. Z. Shen, Strain-driven self-rolling mechanism for anomalous coiling of multilayer nanohelices, *J. Appl. Phys.* **106**, 114314 (2009).
- [149] Y. Forterre and J. Dumais, Generating helices in nature, *Science* **333**, 1715 (2011).
- [150] J. T. Pham, J. Lawrence, D. Y. Lee, G. M. Grason, T. Emrick, and A. J. Crosby, Highly stretchable nanoparticle helices through geometric asymmetry and surface forces, *Adv. Mater.* **25**, 6703 (2013).
- [151] Z. L. Wu, M. Moshe, J. Greener, H. Therien-Aubin, Z. H. Nie, E. Sharon, and E. Kumacheva, Three-dimensional shape transformations of hydrogel sheets induced by small-scale modulation of internal stresses, *Nat. Commun.* **4**, 1586 (2013).
- [152] J. Bae, J. H. Na, C. D. Santangelo, and R. C. Hayward, Edge-defined metric buckling of temperature-responsive hydrogel ribbons and rings, *Polymer* **55**, 5908 (2014).
- [153] M. Godinho, J. Canejo, G. Feio, and E. Terentjev, Self-winding of helices in plant tendrils and cellulose liquid crystal fibers, *Soft Matter* **6**, 5965 (2010).
- [154] J. P. Canejo and M. H. Godinho, Cellulose perversions, *Materials* **6**, 1377 (2013).
- [155] X. Y. Ji, M. Q. Zhao, F. Wei, and X. Q. Feng, Spontaneous formation of double helical structure due to interfacial adhesion, *Appl. Phys. Lett.* **100**, 263104 (2012).
- [156] T. J. Matray and E. T. Kool, A specific partner for abasic damage in DNA, *Nature (London)* **399**, 704 (1999).
- [157] P. Wittung, P. E. Nielsen, O. Buchardt, M. Egholm, and B. Norden, DNA-like double helix formed by peptide nucleic-acid, *Nature (London)* **368**, 561 (1994).
- [158] J. Liu, X. Zhang, Y. J. Zhang, X. H. Chen, and J. Zhu, Nano-sized double helices and braids: Interesting carbon nanostructures, *Mater. Res. Bull.* **38**, 261 (2003).
- [159] M. Q. Zhao, J. Q. Huang, Q. Zhang, J. Q. Nie, and F. Wei, Stretchable single-walled carbon nanotube double helices derived from molybdenum-containing layered double hydroxides, *Carbon* **49**, 2148 (2011).
- [160] Q. Zhang, M. Q. Zhao, D. M. Tang, F. Li, J. Q. Huang, B. L. Liu, W. C. Zhu, Y. H. Zhang, and F. Wei, Carbon-nanotube-array double helices, *Angew. Chem., Int. Ed.* **49**, 3642 (2010).
- [161] J. Kim, J. A. Hanna, M. Byun, C. D. Santangelo, and R. C. Hayward, Designing responsive buckled surfaces by half-tone gel lithography, *Science* **335**, 1201 (2012).
- [162] B. Simpson, G. Nunnery, R. Tannenbaum, and K. Kalaitzidou, Capture/release ability of thermo-responsive polymer particles, *J. Mater. Chem.* **20**, 3496 (2010).
- [163] K. Kalaitzidou and A. J. Crosby, Adaptive polymer particles, *Appl. Phys. Lett.* **93**, 041910 (2008).
- [164] A. Agrawal, T. Yun, S. L. Pesek, W. G. Chapman, and R. Verduzco, Shape-responsive liquid crystal elastomer bilayers, *Soft Matter* **10**, 1411 (2014).
- [165] Q. Ge, C. K. Dunn, H. J. Qi, and M. L. Dunn, Active origami by 4D printing, *Smart Mater. Struct.* **23**, 094007 (2014).
- [166] S. Xu *et al.*, Assembly of micro/nanomaterials into complex, three-dimensional architectures by compressive buckling, *Science* **347**, 154 (2015).
- [167] T. Delclos, C. Aime, E. Pouget, A. Brizard, I. Huc, M. H. Delville, and R. Oda, Individualized silica nanohelices and nanotubes: Tuning inorganic nanostructures using lipidic self-assemblies, *Nano Lett.* **8**, 1929 (2008).
- [168] Z. Chen, Shape transition and multi-stability of helical ribbons: A finite element method study, *Arch. Appl. Mech.* **85**, 331 (2015).
- [169] Z. Chen, Geometric nonlinearity and mechanical anisotropy in strained helical nanoribbons, *Nanoscale* **6**, 9443 (2014).
- [170] S. Cranford and M. J. Buehler, Twisted and coiled ultra-long multilayer graphene ribbons, *Model Simul. Mater. Sci. Eng.* **19**, 054003 (2011).
- [171] H. S. Lee, M. Cho, and B. J. Lee, Size dependence in self-bending mechanism of Ge/Si bilayer nanofilms, *J. Appl. Phys.* **109**, 074314 (2011).
- [172] O. O. Kit, T. Tallinen, L. Mahadevan, J. Timonen, and P. Koskinen, Twisting graphene nanoribbons into carbon nanotubes, *Phys. Rev. B* **85**, 085428 (2012).
- [173] H. Therien-Aubin, Z. L. Wu, Z. H. Nie, and E. Kumacheva, Multiple shape transformations of composite hydrogel sheets, *J. Am. Chem. Soc.* **135**, 4834 (2013).

- [174] S. Iamsaard, S. J. Asshoff, B. Matt, T. Kudernac, J. J. L. M. Cornelissen, S. P. Fletcher, and N. Katsonis, Conversion of light into macroscopic helical motion, *Nat. Chem.* **6**, 229 (2014).
- [175] L. T. de Haan, J. M. N. Verjans, D. J. Broer, C. W. M. Bastiaansen, and A. P. H. J. Schenning, Humidity-responsive liquid crystalline polymer actuators with an asymmetry in the molecular trigger that bend, fold, and curl, *J. Am. Chem. Soc.* **136**, 10585 (2014).
- [176] R. M. Erb, J. S. Sander, R. Grisch, and A. R. Studart, Self-shaping composites with programmable bioinspired microstructures, *Nat. Commun.* **4**, 1712 (2013).
- [177] A. Goriely and M. Tabor, Spontaneous Helix Hand Reversal and Tendril Perversion in Climbing Plants, *Phys. Rev. Lett.* **80**, 1564 (1998).
- [178] T. McMillen and A. Goriely, Tendril perversion in intrinsically curved rods, *J. Nonlinear Sci.* **12**, 241 (2002).
- [179] J. Liu, J. S. Huang, T. X. Su, K. Bertoldi, and D. R. Clarke, Structural transition from helices to hemihelices, *PLoS One* **9**, e93183 (2014).
- [180] Y. Forterre, J. M. Skotheim, J. Dumais, and L. Mahadevan, How the Venus flytrap snaps, *Nature (London)* **433**, 421 (2005).
- [181] D. P. Holmes and A. J. Crosby, Snapping surfaces, *Adv. Mater.* **19**, 3589 (2007).
- [182] H. Lee, C. G. Xia, and N. X. Fang, First jump of microgel; actuation speed enhancement by elastic instability, *Soft Matter* **6**, 4342 (2010).
- [183] M. R. Shankar, M. L. Smith, V. P. Tondiglia, K. M. Lee, M. E. McConney, D. H. Wang, L.-S. Tan, and T. J. White, Contactless, photoinitiated snap-through in azobenzene-functionalized polymers, *Proc. Natl. Acad. Sci. U.S.A.* **110**, 18792 (2013).
- [184] T. G. Leong, C. L. Randall, B. R. Benson, N. Bassik, G. M. Stern, and D. H. Gracias, Tetherless thermobiochemically actuated microgrippers, *Proc. Natl. Acad. Sci. U.S.A.* **106**, 703 (2009).
- [185] Z. Chen, Q. H. Guo, C. Majidi, W. Z. Chen, D. J. Srolovitz, and M. P. Haataja, Nonlinear Geometric Effects in Mechanical Bistable Morphing Structures, *Phys. Rev. Lett.* **109**, 114302 (2012).
- [186] S. D. Guest, E. Kebabze, and S. Pellegrino, A zero-stiffness elastic shell structure, *J. Mech. Mater. Struct.* **6**, 203 (2011).
- [187] K. A. Seffen and S. D. Guest, Prestressed morphing bistable and neutrally stable shells, *J. Appl. Mech.* **78**, 011002 (2011).
- [188] E. H. Mansfield, Bending buckling, and curling of a heated elliptical plate, *Proc. R. Soc. A* **288**, 396 (1965).
- [189] L. B. Freund, Substrate curvature due to thin film mismatch strain in the nonlinear deformation range, *J. Mech. Phys. Solids* **48**, 1159 (2000).
- [190] Q. Guo, H. Zheng, W. Chen, and Z. Chen, Modeling bistable behaviors in morphing structures through finite element simulations, *Bio-medical Mater. Eng.* **24**, 557 (2014).
- [191] X. Lachenal, P. Weaver, and S. Daynes, Multistable composite twisting structure for morphing applications, *Proc. R. Soc. A* **468**, 1230 (2012).
- [192] A. Pirrera, X. Lachenal, S. Daynes, P. M. Weaver, and I. V. Chenchiah, Multi-stable cylindrical lattices, *J. Mech. Phys. Solids* **61**, 2087 (2013).
- [193] N. Hu and R. Burgueño, Buckling-induced smart applications: Recent advances and trends, *Smart Mater. Struct.* **24**, 063001 (2015).
- [194] T. Ohzono and M. Shimomura, Ordering of microwrinkle patterns by compressive strain, *Phys. Rev. B* **69**, 132202 (2004).
- [195] T. Ohzono and M. Shimomura, Geometry-dependent stripe rearrangement processes induced by strain on preordered microwrinkle patterns, *Langmuir* **21**, 7230 (2005).
- [196] T. Ohzono, Control of cooperative switching of microwrinkle orientations by nanopatterns, *Chaos* **19**, 033104 (2009).